A new geological slip rate estimate for the Calico Fault, eastern California: implications for geodetic versus geologic rate estimates in the Eastern California Shear Zone

Surui Xie, Elisabeth Gallant, Paul H. Wetmore, Paula M. Figueiredo, Lewis A. Owen, Craig Rasmussen, Rocco Malservisi & Timothy H. Dixon

Taylor & Francis
Taylor & Francis Group

ARTICLE

Check for updates

A new geological slip rate estimate for the Calico Fault, eastern California: implications for geodetic versus geologic rate estimates in the Eastern California Shear Zone

Surui Xie [a], Elisabeth Gallant [a], Paul H. Wetmore[a], Paula M. Figueiredo [b], Lewis A. Owen [b], Craig Rasmussen [c], Rocco Malservisi [a] and Timothy H. Dixon [a]

[a]School of Geosciences, University of South Florida, Tampa, FL, USA; [b]Department of Geology, University of Cincinnati, Cincinnati, OH, USA; [c]Department of Soil, Water and Environmental Science, University of Arizona, Tucson, AZ, USA

ABSTRACT

Accurate estimation of fault slip rate is fundamental to seismic hazard assessment. Previous work suggested a discrepancy between short-term geodetic and long-term geologic slip rates in the Mojave Desert section of the Eastern California Shear Zone (ECSZ). Understanding the origin of this discrepancy can improve understanding of earthquake hazard and fault evolution. We measured offsets in alluvial fans along the Calico Fault near Newberry Springs, California, and used several techniques to date the offset landforms and determine a slip rate. Our preferred slip rate estimate is 3.2 ± 0.4 mm/yr, representing an average over the last few hundred thousand years, faster than previous estimates. Seismic hazard associated with this fault may therefore be higher than previously assumed. We discuss possible biases in the various slip rate estimates and discuss possible reasons for the rate discrepancy. We suggest that the ECSZ discrepancy is an artefact of limited data, and represents a combination of faster slip on the Calico Fault, off-fault deformation, unmapped fault strands, and uncertainties in the geologic rates that have been underestimated. Assuming our new rate estimate is correct and a fair amount (40%) of off-fault deformation occurs on major ECSZ faults, the summed geologic rate estimate across the Mojave section of the ECSZ is 10.5 ± 3.1 mm/yr, which is equivalent within uncertainties to the geodetic rate estimate.

1. Introduction

The slip rate of an active fault is a fundamental parameter in seismic hazard estimation (Petersen et al. 2015). Knowledge of strain partitioning and slip rate accommodation across a plate boundary zone is also important for understanding how faults evolve and interact with other faults (Dolan et al. 2007; Ye and Liu 2017; Dixon and Xie 2018). Fault slip rate can vary in both space and time, potentially affecting the timing and magnitude of future damaging earthquakes, emphasizing the importance of detailed studies.

The Eastern California Shear Zone (ECSZ) accommodates ~20–25% of Pacific-North America plate motion in central and southern California, northeast of the Big Bend of the San Andreas Fault (Dokka and Travis 1990a, 1990b; Sauber et al. 1994; Dixon et al. 1995, 2000; Miller et al. 2001; Lifton et al. 2013; Figure 1). Most of the remaining plate motion is accommodated to the west, on the San Andreas Fault in central California, or the San Andreas, San Jacinto, and Elsinore faults in southern California (e.g. Bennett et al. 1996; Meade and Hager 2005; Shen et al. 2011). Formation of the ECSZ is kinematically linked to the Big Bend, whose formation in turn is related to the inland jump of the southern part of the plate boundary at ~5–10 Ma (Atwater and Stock 1998; McQuarrie and Wernicke 2005). Several faults within the ECSZ likely formed or accelerated around this time or later (Dokka and Travis 1990a, 1990b).

The region has been an important natural laboratory to study the formation and evolution of faults (Frankel et al. 2008), as well as other tectonic and plate kinematic studies. Dokka and Travis (1990a, 1990b), Savage et al. (1990) and Sauber et al. (1994) recognized the importance of the ECSZ in accommodating a significant fraction of Pacific-North America plate motion. Minster and Jordan (1987) first identified the 'San Andreas discrepancy'; the discrepancy represents the difference between overall plate motion and motion carried by the San Andreas Fault. The discrepancy was initially
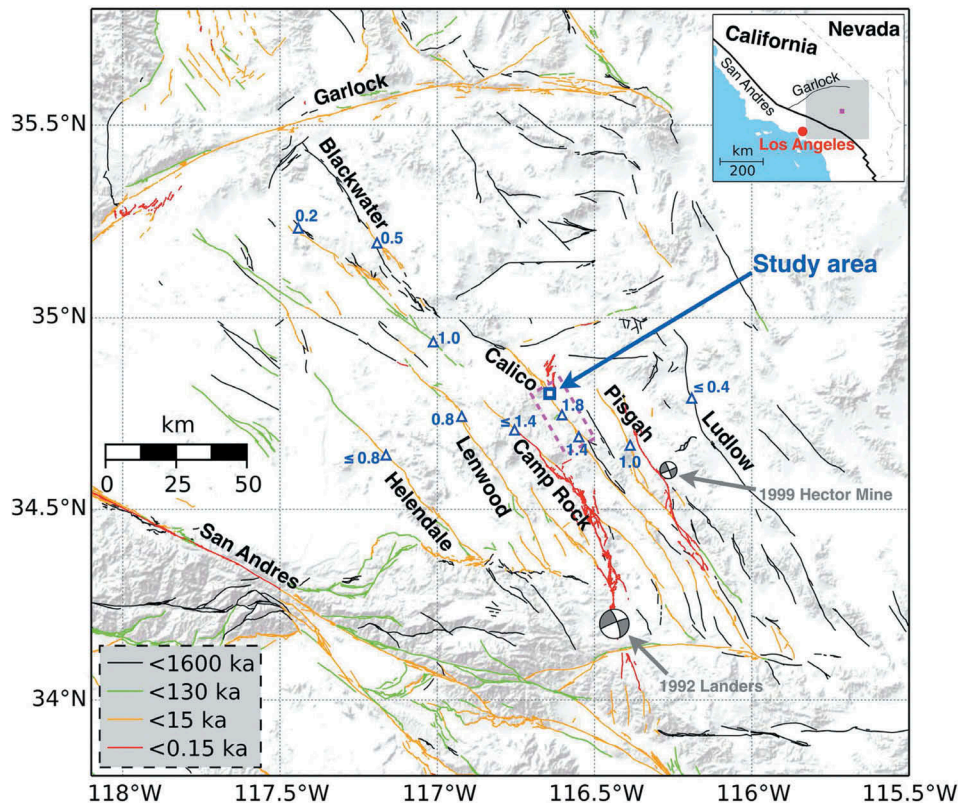
Figure 1. Fault map showing the ECSZ in the Mojave Desert, from U.S. Geological Survey and California Geological Survey (2006). Colour indicates time of recent movement. Blue triangles show locations of geologic strike-slip rate estimates from recent studies, with rates given in mm/yr (Oskin and Iriondo 2004; Oskin *et al*. 2007a, 2008; Selander 2015). Beach balls mark the 1992 M_w 7.3 Landers earthquake and the 1999 M_w 7.1 Hector Mine earthquake. Blue square shows our study site. Dashed magenta box outlines the area of Figure 15(b). Selected fault names are labelled beside corresponding faults. Insert: Grey outlines area shown in the main figure. Red dot marks Los Angeles. Magenta square indicates location of the outlined magenta box in the main figure (corresponding to the area shown in Figure 15(b)).

attributed to significant right-lateral shear on other faults within the Basin and Range province to the east and the California continental margin to the west (Minster and Jordan 1987; Ward 1990). Improvements in geodetic data in the last few decades have clarified slip partitioning across the entire Pacific-North America plate boundary and suggest a general agreement between summed geodetic slip rates across individual deforming zones and overall relative plate motion (e.g. DeMets and Dixon 1999; Sella *et al*. 2002; Kreemer *et al*. 2003; DeMets and Merkouriev 2016).

More recently, several researchers (e.g. Gan *et al*. 2000; Meade and Hager 2005; Oskin *et al*. 2008; Spinler *et al*. 2010; Evans *et al*. 2016) have noted discrepancies between geologically determined and geodetically determined slip rate estimates for individual faults within the ECSZ, or for summed rates across the shear zone, hereafter termed the ECSZ discrepancy. For example, in the Mojave Desert region (Figure 1), the summed geologic slip rate across the region at ~34.8°N has been defined as ≤6.2 ± 1.9 mm/yr (Oskin *et al*.

2008), while geodetic rate estimates are significantly faster, ~11 to ~18 mm/yr (Evans *et al*. 2016 and references therein) (Figure 2). A variety of factors could contribute to the ECSZ discrepancy, including:

(1) Off-fault deformation, such that fault slip rates *sensu stricto* are less than the integrated block motion rate across the larger fault zone (e.g. Shelef and Oskin 2010; Dolan and Haravitch 2014; Herbert *et al*. 2014a).
(2) Acceleration of young, immature faults (Gourmelen *et al*. 2011), such that the geologic rate, which may average over the early stages of a fault zone's activity, will be less than the current rate measured by geodesy.
(3) Temporal changes in fault slip rates beyond simple acceleration, reflecting complex tectonic processes in the ECSZ, including transient strain on individual faults or temporally clustered earthquakes at the scale of the shear zone (Rockwell *et al*. 2000; Peltzer *et al*. 2001; Oskin and Iriondo 2004; Meade and
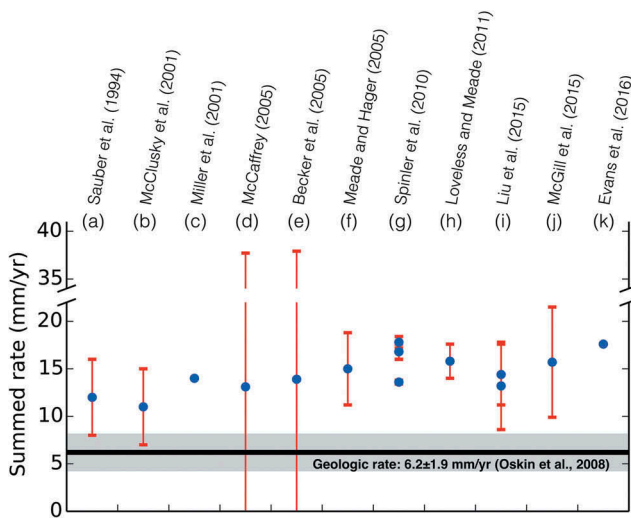
Figure 2. Summed geodetic and geologic rates across the ECSZ. Black line and grey area mark the summed geologic slip rate and uncertainty (95% confidence) from Oskin *et al.* (2008). Blue dots with error bars represent summed geodetic rates and their uncertainties (also 95% confidence) from elastic deformation models (a)–(k). Slip rates for (d) (McCaffrey 2005) and (h) (Loveless and Meade 2011) calculated at latitude 34.8° N based on their block models. Spinler *et al.* (2010) and Liu *et al.* (2015) provide multiple solutions. Miller *et al.* (2001) and Evans *et al.* (2016) did not provide uncertainties.

Hager 2005; Dolan *et al.* 2007; Oskin *et al.* 2007a, 2008; Cooke and Dair 2011; Dixon and Xie 2018).

(4) The effects of post-seismic motion and visco-elastic relaxation, such that geodetic rates within a few decades of a major earthquake are faster than their long-term average (Dixon *et al.* 2003; Chuang and Johnson 2011; McGill *et al.* 2015). In other words, the rates differ only because the long-term rate is not properly modelled in some geodetic approaches, for example, those that assume purely elastic rheology.

(5) Unmapped faults

(6) Systematic errors in one or both of the geodetic and geologic techniques.

Determining the origin of such discrepancies, in the ECSZ and elsewhere, is important for a variety of reasons, including improved understanding of earthquake process and fault evolution, as well as seismic hazard assessment. In its simplest form, the potential seismic hazard for a given fault is positively correlated with the fault's slip rate: in a given period of time, faults with higher slip rates are loaded faster than faults with lower slip rates (Petersen *et al.* 2015). Accurate estimation of a fault's current slip rate, and possible long-term variation, is paramount.

Geological slip rate estimates suffer from a limited database. Bird (2007) investigated slip rate data for >800 faults in the conterminous western United States and found that only a small portion (~6%) have well-constrained rates (having combined probability density functions for long-term slip rate in which the width of the 95% confidence range is smaller than the median). He argued that ~4 offset features are required to achieve a well-constrained rate, and ≥7 offset features are required to guarantee a high degree of certainty. To our knowledge no fault in the Mojave ECSZ region has been studied sufficiently to meet Bird's (2007) criteria and generate the necessary ensemble of rate estimates (Oskin *et al.* 2008 and references therein).

There are two other issues relevant to slip rate characterization: (1) Surface displacement can be heterogeneous along a fault, perhaps representing interactions between neighbouring faults or different levels of off-fault deformation (e.g. Dolan and Haravitch 2014; Fletcher *et al.* 2014); and (2) precise dating of offset features can be challenging, especially for Pleistocene and younger alluvial fans (a common offset marker), where surface exposure dating techniques typically exhibit a high degree of scatter. Consequently, a given slip-rate estimate may not be robust, emphasizing the importance of additional studies.

Here, we review geodetic and geologic slip rate estimates for the region and report a new geological slip rate estimate for the Calico Fault, a major fault within the Mojave Desert section of the ECSZ. The new rate is significantly faster than previously determined geologic slip rates, and hence bears on the issue (and perhaps the reality) of the ECSZ discrepancy.

2. Previous work

2.1. Prior geodetic studies

Fault slip rate estimates based on geodetic data are model-dependent. Most models assume either a purely elastic rheology or an elastic layer overlying on one or more visco-elastic layers. The latter has been used to study earthquake-cycle effects in several parts of the Pacific-North America boundary zone (Malservisi *et al.* 2001, 2003; Schmalzle *et al.* 2005; Fulton *et al.* 2010; Chuang and Johnson 2011). Dixon *et al.* (2003), McGill *et al.* (2015) and Evans *et al.* (2016) suggested that discrepancies between geodetic and geologic slip rates in the ECSZ and Walker Lane (the northern continuation of the ECSZ) could be caused by prior earthquakes which stimulate visco-elastic deformation in the lower crust and upper mantle that varies over the time scale of an earthquake cycle. Liu *et al.* (2015) used

historical triangulation/trilateration observations before the 1992 Landers earthquake and GPS measurements after the Landers earthquake to recover the secular deformation field and differentiate post-seismic transients. They found that the 1992 Landers and 1999 Hector Mine earthquakes adversely affect GPS measurements, with 2–3 mm/yr excess right-lateral shear inferred across the co-seismic ruptures in the post-earthquake GPS solutions. They estimate a cumulative long-term deformation rate of 13.2–14.4 mm/yr across the Mojave section of the ECSZ, similar within uncertainties to the pre-Landers geodetic estimate of 12 mm/yr by Sauber *et al.* (1994).

Herbert *et al.* (2014b) used a boundary element method to simulate three-dimensional deformation of the ECSZ. Their modelling approach suggests that a block-like fault network (faults are simplified to be connected) can produce a cumulative strike-slip rate estimate that is 36% greater than a discontinuous fault model. Based on gradients in the derived deformation map and the implied strain energy density, Herbert *et al.* (2014a) concluded that 40 ± 23% of the total strain across the ECSZ could be attributed to off-fault deformation.

Evans *et al.* (2016) used a total variation regularization method to investigate the role of fault system geometry in block models, determining a best-fitting geometry from an initial model with numerous faults. This method minimizes the influence of fault geometry assumptions and reduces uncertainties in geodetic slip rate estimates. Moreover, since a dense fault geometry was used in the initial model, which included active faults separated by <10 km, this modelling method should be able to assess the role of distributed deformation. Evans *et al.* (2016) identified persistent discrepancies between geologically and geodetically estimated slip rates in the ECSZ, with 4–7 mm/yr discrepancies on the Calico Fault. This suggests the importance of additional studies of the Calico Fault.

To the north of the ECSZ in the southern Walker Lane, across the Northern Death Valley-Fish Lake Valley Fault (DV-FLVF) and the White Mountain Fault (WMF), Lifton *et al.* (2013) compared GPS-based crustal velocities and geologic slip rates, and found that most of the observed discrepancy between long- and short-term slip rates occurs across Owens Valley. They concluded that the observed geodetic versus geologic discrepancy across the southern Walker Lane is likely a combination of under-estimated geologic slip rates on the WMF and broadly distributed deformation in Owens Valley that is not well preserved in the geologic record.

2.2. Prior geologic studies

From analysis of paleoseismologic trench data and offset landforms along the Calico Fault near Newberry Springs, California, Ganev *et al.* (2010) found that strain release on the Calico Fault has been highly episodic over the past ~9000 yr, reinforcing the suggestion that earthquakes in the ECSZ are clustered (e.g. Rockwell *et al.* 2000; Dolan *et al.* 2007). The geomorphic displacements in the paleoseismologic evidence along the Calico Fault imply that more than one large earthquake ($M_w \geq 7.0$) can occur in each clustering time period (Ganev *et al.* 2010).

Based on a fault initiation time between ~10.6 and 5.5 Ma and a total of 65 km right-lateral displacement at 35° N (from offset Early Miocene markers and a reconstruction model), Dokka and Travis (1990a, 1990b) estimated an integrated long-term slip rate for the ECSZ at 6–12 mm/yr. Assuming that the ECSZ is kinematically linked to the Big Bend in the San Andreas Fault and the inland jump of the plate boundary to the present Gulf of California, age constraints on the timing of the inland jump and the timing of the initiation of marine sedimentation in the northern and southern Gulf of California allow refinement of this estimate. Oskin and Stock (2003) dated marine incursion into the southern Gulf of California at 8.2 Ma, while the northern Gulf is somewhat younger, 6.3–6.5 Ma, perhaps constraining the rate of northward propagation of the developing rift. Bennett *et al.* (2015) refined the age estimate of marine incursion into the northern Gulf, dating it at 6.2 ± 0.2 Ma. The ECSZ likely formed or accelerated shortly after this time. Initiation ages for the ECSZ between 5.0 and 6.0 Ma allow for the possibility of some finite period for northward propagation. Using the 65 km displacement estimate of Dokka and Travis (1990a, 1990b) and this range of initiation ages the long-term average rate for the ECSZ of 10.8–13.0 mm/yr, essentially identical to most of the geodetic estimates within uncertainties.

Oskin *et al.* (2007a, 2008) measured surface displacements across several alluvial fans and a lava flow with different ages, determining the slip rates of six dextral faults (Helendale, Lenwood, Camp Rock, Calico, Pisgah, and Ludlow) across the ECSZ, with an overall rate of ≤6.2 ± 1.9 mm/yr at ~34.8°N. The Calico Fault had the fastest slip rate in these studies, 1.8 ± 0.3 mm/yr. This slip rate is based on a 56.4 ± 7.7 ka old surface offset near Sheep Spring Wash in the northern Rodman Mountains. In a study area located ~8 km southeast of that of Oskin *et al.* (2007a), Selander (2015) estimated a $1.4\ ^{+0.8}/_{-0.4}$ mm/yr slip rate for the Calico Fault based on

a 17.1 $^{+1.6}/_{-2.6}$ ka old surface offset southwest of the Rodman Mountains. Farther north, Oskin and Iriondo (2004) estimated a slip rate of 0.5 mm/yr for the Blackwater Fault, north of the Calico-Blackwater Fault system. Selander (2015) interpreted such rate fluctuations as evidence for strain transfer from the Calico Fault onto other several nearby faults, with overall dextral slip of the ECSZ apparently decreasing to the northwest, to ≤2.6 ± 1.9 mm/yr north of 35°N.

A highly disconnected fault network in the ECSZ could imply significant off-fault deformation (Herbert *et al*. 2014a, 2014b; Selander 2015), or some amount of slip on fault strands that have not been studied. Using the deflection of continuous planar markers and the rotation of paleomagnetic sites, Shelef and Oskin (2010) found that distributed deformation over zones of 1–2 km width accommodates 0 to ~25% of the total displacement, with most displacement occurring within 100–200 m of faults, decreasing nonlinearly away from the fault.

2.3. The role of fault maturity

Wesnousky (1988) found that the structural complexity of strike-slip faults decreased with increasing offset. Several studies of ECSZ faults (e.g., Stirling *et al*. 1996; Rockwell *et al*. 2000; Dolan and Haravitch 2014; Selander 2015) emphasize their structural complexity, a key marker of immaturity, and one that could affect the measurement and interpretation of geologically defined slip rates.

Wesnousky (2005) compared the San Andreas and ECSZ faults systems, noting the latter's smaller cumulative offset and defining it as an immature fault system. Dolan and Haravitch (2014) analysed a global set of large strike-slip earthquakes and found that faults with total offsets ≤ 25 km manifest only ~50–60% of earthquake slip as surface faulting, while faults with total offsets ≥ 85 km display ~85–95% of their slip on surface faults. Based on the inefficiency of generating surface faulting, the authors define strike-slip faults with ≤25 km total offset as immature faults. By this definition, all active faults in the Mojave section of the ECSZ are immature (Dokka 1983; Dokka and Travis 1990a; Dixon and Xie 2018). For example, using well-defined markers from an early Miocene structural belt, Dokka (1983) estimated total offsets on individual active faults across the central Mojave Desert from 1.5 to 14.4 km. On the eastern margin of the ECSZ, the Bristol-Granite Mountain Fault has a total offset of 24 km (Lease *et al*. 2009), but it is currently inactive. The Calico Fault has a total offset of 9.8 km (Glazner *et al*. 2000; Oskin *et al*. 2007a).

While individual faults tend to lengthen, narrow, and simplify with cumulative offset (Wesnousky 1988; Dolan and Haravitch 2014), plate boundary zones as a whole can grow in width and complexity (e.g. by adding new faults) depending on overall plate motion and other kinematic boundary conditions. Oldow *et al*. (2008) describe evolution of the southern Walker Lane, generally considered the northern extension of the ECSZ, and note that parts of it have widened since the Pliocene.

3. New displacement observations

Our study area is located near Newberry Springs, California (Figure 1). Two alluvial fan surfaces here are offset by the Calico Fault (Figure 3). We refer to them as the Autumn Leaf Road (ALR) and Troy Road (TR) alluvial fans based on nearby roads. We estimated their strike-slip displacements based on three data sets: (1) our own field observations including mapped fault scarps; (2) high-resolution aerial ortho-imagery with 0.3 m horizontal resolution, downloaded from USGS EarthExplorer: https://earthexplorer.usgs.gov/; and (3) a digital elevation model (DEM) derived from airborne LiDAR data with 0.5 m horizontal resolution and centimetre-level vertical precision, downloaded from OpenTopography Facility (http://www.opentopography.org/). Aerial ortho-imagery and LiDAR are especially useful in this semi-arid environment.

3.1. ALR alluvial fan

The ALR alluvial fan is the oldest observed alluvial fan surface in the Newberry Springs area and consists of a series of isolated alluvial surfaces elevated 2–6 m above younger surfaces (Figures 3–5). The surface of this alluvial fan is defined by a well-developed desert pavement, dominated by dark varnished pebbles and abundant, widely spaced metre-scale, sub-angular boulders with compositions that include quartzite, basalt, granite and rhyolite (Supplementary Figure S1). Fault traces identified by field mapping and aerial photography show a well-defined linear trace striking ~323°. The Calico Fault displaces the alluvial fan in a right-lateral sense, with the main body (better preserved) on the northeast wall and three smaller bodies (remnants, partially eroded) on the southwest wall, ~1 km to the northwest of the main body. The alluvial fan surface is characterized by shallow (0–2 m deep) channels that are partially filled by deposit and boulders, with one prominent (1–2 m deep) drainage on both the main body and the northwestern-most of the three smaller bodies (marked by red dots in Figure 4(b)). Excavation of two 2-m-deep, 1-m-wide, and 2-m-long trenches (CalicoA and Calico-Pit3,
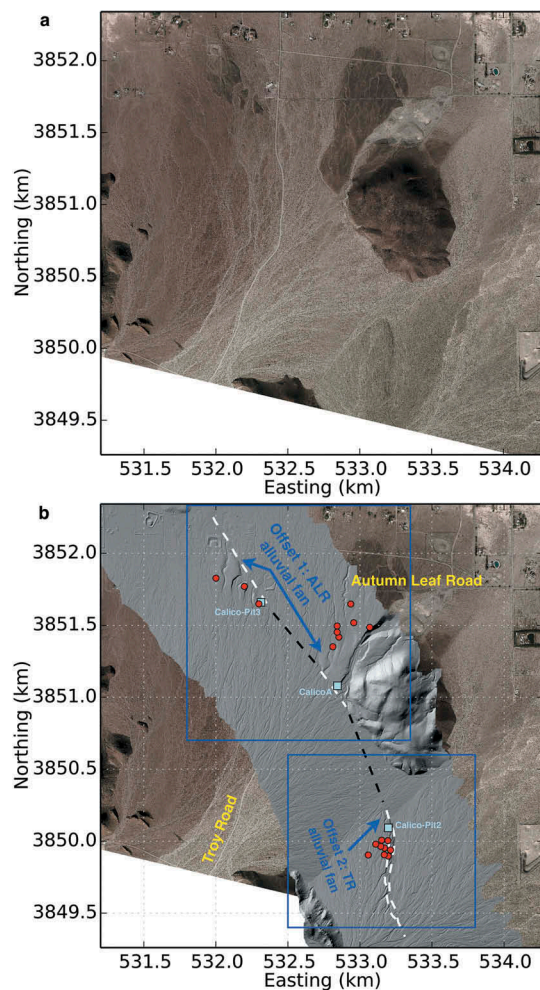
Figure 3. Images of the study area. (a) Aerial ortho-image. (b) LiDAR hillshade overlain on aerial image. Blue boxes outline two offset landforms shown in Figures 5 (ALR alluvial fan) and 7 (TR alluvial fan). Dashed white lines indicate mapped fault traces, dashed black lines are inferred fault traces. Red dots show locations of rock samples. Light blue squares are trench or locations: CalicoA and Calico-Pit3 on the ALR alluvial fan and Calico-Pit2 on the TR alluvial fan. Coordinates are in UTM zone 11 N.

locations shown in Figure 3(b)) into the side of the ALR alluvial fan reveals that the deposit is dominated by cobbles and occasional boulders, with well-developed calcium carbonate coatings at depths > 0.2 m. The coatings are <4 mm (typically 0.5–2 mm) in thickness (Supplementary Figure S2), with some weak conjoining of adjacent clasts.

We reconstructed the pre-displacement ALR alluvial fan along the fault trace based on surface features and the LiDAR DEM, obtaining 1110 ± 110 m (2σ uncertainty is used in this paper) of right-lateral displacement (Figures 4 and 5). This places the largest of the three smaller alluvial fan bodies immediately adjacent to the southwestern margin of the main body. This also aligns the wide paleo-channel (between the cyan and yellow dots in Figure 4(b))

on both sides of the fault, and the prominent drainage on the alluvial fan surfaces (marked by red dots in Figure 4(b)). We note that this reconstruction aligns a paleo-creek strongly incised in the remnants of the alluvial fan in the northwest to the prominent drainage present on the southeastern alluvial fan body. This southeastern drainage starts deeply incised into the alluvial fan body but drains to the northeast. There is no topographic or geomorphologic reason for this, while the paleo-creek on the northwest alluvial fan body does not seem to have a continuation across the fault trace (Figures 3 and 4). Thus, we interpret the prominent drainage as a pre-existing drainage that was once related to the dominant drainage on the northwester fan body. The width of the channel to the southeast of the major body (110 m) is used to define the uncertainty for this displacement, following the method of Frankel *et al.* (2011). We used several methods and tools to analyse the geomorphology in detail and interpret the displaced features, including the software package LaDiCaoz (v2.1) (Zielke *et al.* 2015; Haddon *et al.* 2016) (Figure 6). By shifting an elevation profile 25 m southwest from the fault (red line between two yellow dots in Figure 6(a)) along the fault trace, an 1111 m horizontal displacement minimizes misfit (Figure 6(d)) to the elevation profile northeast of the fault (solid blue line in Figure 6(a)), with a 27.5 m vertical displacement that is perhaps due to southwest-side down dipping of the fault (Selander 2015). Figure 6(f) shows a restored contour map, where sharp-pointed V's near the ALR alluvial fan are well-aligned between the two sides of the fault. Figure 6(g,h) shows two elevation profiles (corresponding to red and blue dotted yellow lines in Figure 6(a)) along the dominant drainage before and after restoration; Figure 6(i,j) shows two elevation profiles (corresponding to dashed red and blue lines in Figure 6(a)) on the fan surfaces before and after restoration. These show that both the dominant drainage and alluvial fan surface on two sides of the fault have a similar slope aspect. Since the software package LaDiCaoz yields a displacement estimate that is virtually identical to the estimate based on reconstructions using aerial ortho-imagery and the LiDAR DEM, we use 1110 ± 110 m as the displacement and corresponding uncertainty for the ALR alluvial fan. While using the selected paleo-channels as piercing points may induce uncertainty to the reconstruction of older alluvial fans due to erosion, we feel this is reflected in our uncertainty estimate.

3.2. TR alluvial fan

The TR alluvial fan is located ~1 km southeast of the main body of the ALR alluvial fan (Figure 3). Here, rock varnish is moderately developed (light brown) on the surface, and desert pavement is not well developed, suggesting an
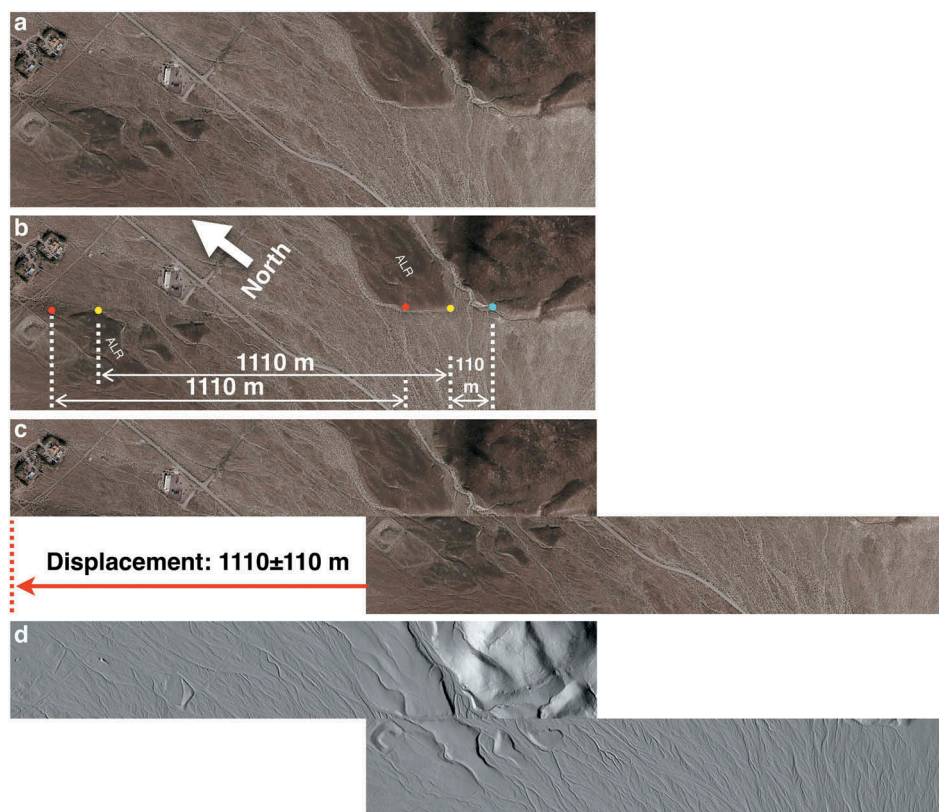
Figure 4. Slip restoration for the ALR alluvial fan. (a) Aerial image of the ALR alluvial fan. (b) The pair of red and yellow dots marked key features used to align offset fan bodies, width of the major channel is used as uncertainty. (c) Restored alluvial fan. (d) Hillshade of the restored alluvial fan.

age that is younger than the ALR alluvial fan, but older than the active channel. A network of partly filled channels and trains of 0.5–1-m-size boulders characterize the alluvial fan surface. Well-preserved bars with imbricated boulders are pervasive across this fan surface. Carbonate coatings and rubification of the undersides of clasts and boulders are indistinct or not developed within this fan on the surface and an evacuated trench (Calico-Pit2, location shown in Figure 3(b)), consistent with a younger age compared to the ALR alluvial fan. The TR alluvial fan is eroded along both its northwestern and southeastern margins, with active channels traversing the alluvial fan from south-southwest to northeast (Figures 7(a) and 8(a)). Surface fault traces show that the Calico Fault transfers slip from south-north to southeast-northwest trend as it passes this alluvial fan and produces some secondary fault traces near the main fault scarp. The main fault strikes ~338° at the northwestern margin of this alluvial fan (Figures 3 and 7; Ganev *et al.* 2010).

Northwest of the TR alluvial fan there is an alluvial surface that exhibits no notable fault scarp, suggesting an age that is intermediate between the TR alluvial fan and the active channel, which has a well-defined easterly-northeasterly dip, as illustrated in the LiDAR DEM.

We term this intermediate alluvial fan surface IAF (Figure 8(e)). The active channel has a narrow reach at the southwest end (black line in Figure 8(e)) and is characterized by a broad, anastomosing stream channel (ASC) reach within ~300 m of the fault on the southwest wall and continuing across the map area on the northeast wall. The ASC has split the active channel into a broad drainage system. Located between the TR alluvial fan and the active channel ASC on the northeast wall is a small (~100 × 300 m) area of this IAF surface that has escaped reworking by the active channel ASC (IAF*, outlined by the yellow dashed in Figure 8(e)). Palaeostream channels across its surface have the same trend as the broader IAF surface. The TR-IAF* boundary likely formed at the same time as or slightly later than the formation of the broader IAF surface, that is, some unknown amount of time after the formation of TR alluvial fan.

The multiple surfaces in close proximity to the TR alluvial fan suggest a complex erosion-deposition history, complicating the interpretation of fault displacement. Assuming the TR-IAF/IAF* boundary had a straight shape at its formation we interpret a displacement between 90 and 200 m, depending on the

Figure 5. Displacement of the ALR alluvial fan (offset 1 outlined in Figure 3(b)). (a) Aerial image of the ALR alluvial fan, red dots mark prominent drainages on alluvial fan surfaces, yellow and cyan dots mark width of major channel used to define uncertainty of displacement estimate. (b) LiDAR hillshade overlain on aerial image, note the prominent drainage on offset fan bodies. (c) Slope aspect derived from LiDAR DEM overlain on aerial image. (d–f) Restoration of 1110 m of right-lateral slip on the Calico Fault, corresponding to present surface features shown in (a–c). (g–h) Elevation contour (white lines) before and after restoration overlain on the hillshade, contour interval is 2 m.

time and degree of incision of the ASC (90 m if the ASC incised exclusively into the IAF, and the current TR-ASC boundary was a maximum extent of the IAF before incision of the ASC; 200 m if the ASC incised exclusively into the TR alluvial fan, and the current southwestern IAF-ASC boundary was the maximum extent of the TR alluvial fan before incision of the ASC (Figures 7(i-p) and 8(c–g)). Both of these interpretations assume that erosion has been equal along the TR edge at both sides of the faults. Since erosion might not have been equal, due to differences in incision or changes in the anastomosing drainage patterns, alternative restorations are possible. Local geometric complexities due to fault steps (e.g. fault bending, vertical deformation, multiple fault strands), could also exert control on surface
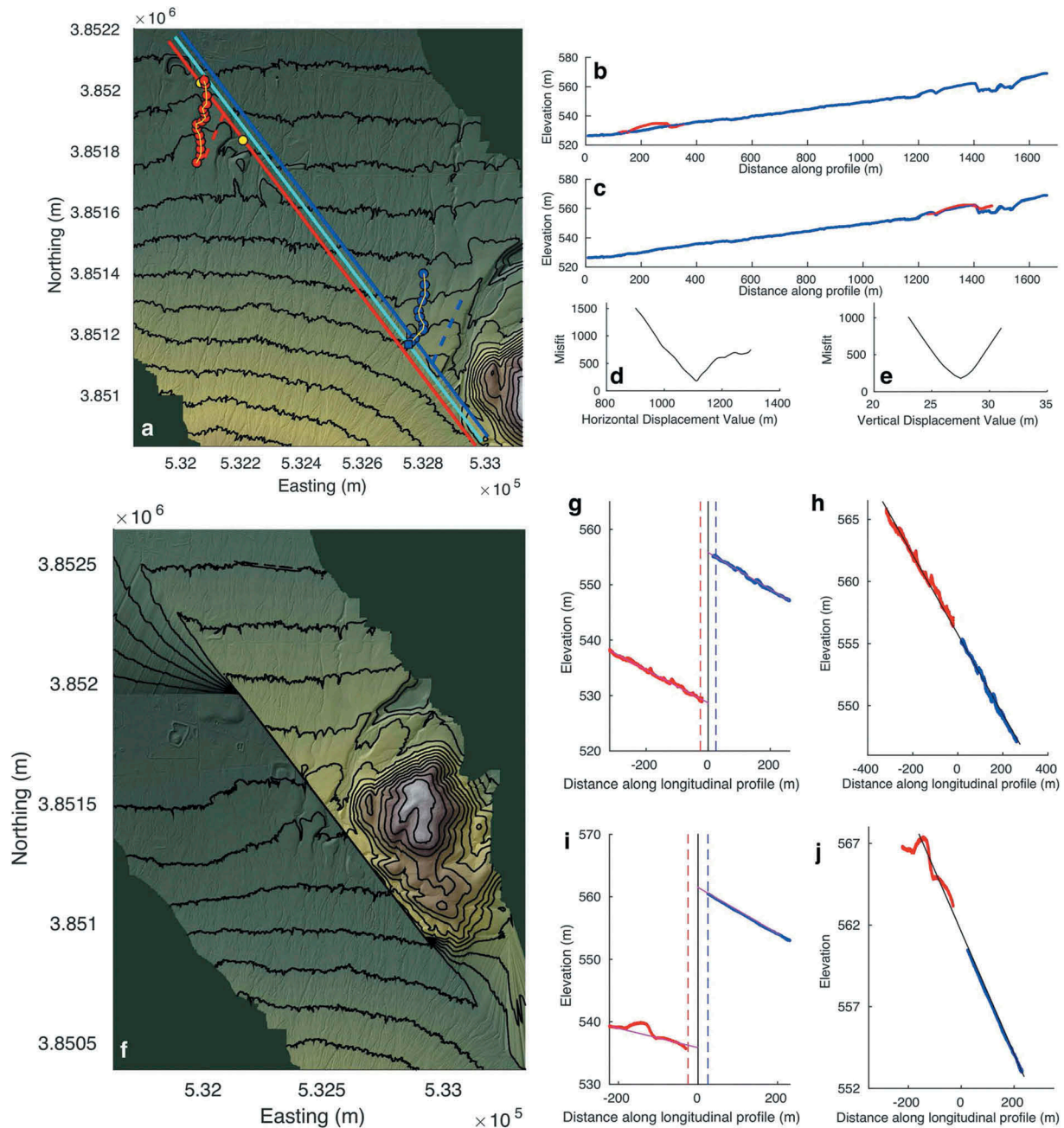
Figure 6. Displacement restoration using LaDiCaoz software (Zielke *et al*. 2015; Haddon *et al*. 2016) for the ALR alluvial fan. (a) Contour of the ALR alluvial fan, 5 m contour interval. Cyan line marks the fault trace, blue line marks an elevation profile shown in (b), red line marks another profile with elevation between the two yellows dots shown in (b). Red and blue dotted lines mark the upstream and downstream limits of the prominent drainage in the fan bodies. (b) Blue line corresponds to the blue line in (a), red line corresponds to the section of the red profile marked by two yellow dots in (a). (c) Best match by shifting the red profile in b, (d–e) shows misfit using different displacements. The best match corresponds to a horizontal displacement of 1111 m. (f) Reconstructed elevation map based on a 1111 m displacement, contours at two ends have some artificial distortion due to the algorithm in the software but will not affect the analysis. (g) Red and blue scatter corresponding to dotted red and blue lines in (a), magenta lines are visually fits of straight lines. Black vertical line corresponds to fault location. Dashed red and blue lines correspond to the red and blue line in (a). (h) Profile of the dominant drainage after restoration. Black line is a reference to examine the straightness of the reconstructed dominant drainage. (i–j) Red and blue scatter corresponding to dashed red and blue lines in (a), the other symbols are the same as in (g) and (h).

processes and mask recognition of features. For example, the edge of the TR alluvial fan may originally have had a more curved shape before the deposition of IAF or the incision of ASC. In that case, the displacement could be <<90 m. Figures 7 (e–h) and 8(b) show a restoration of 20 m
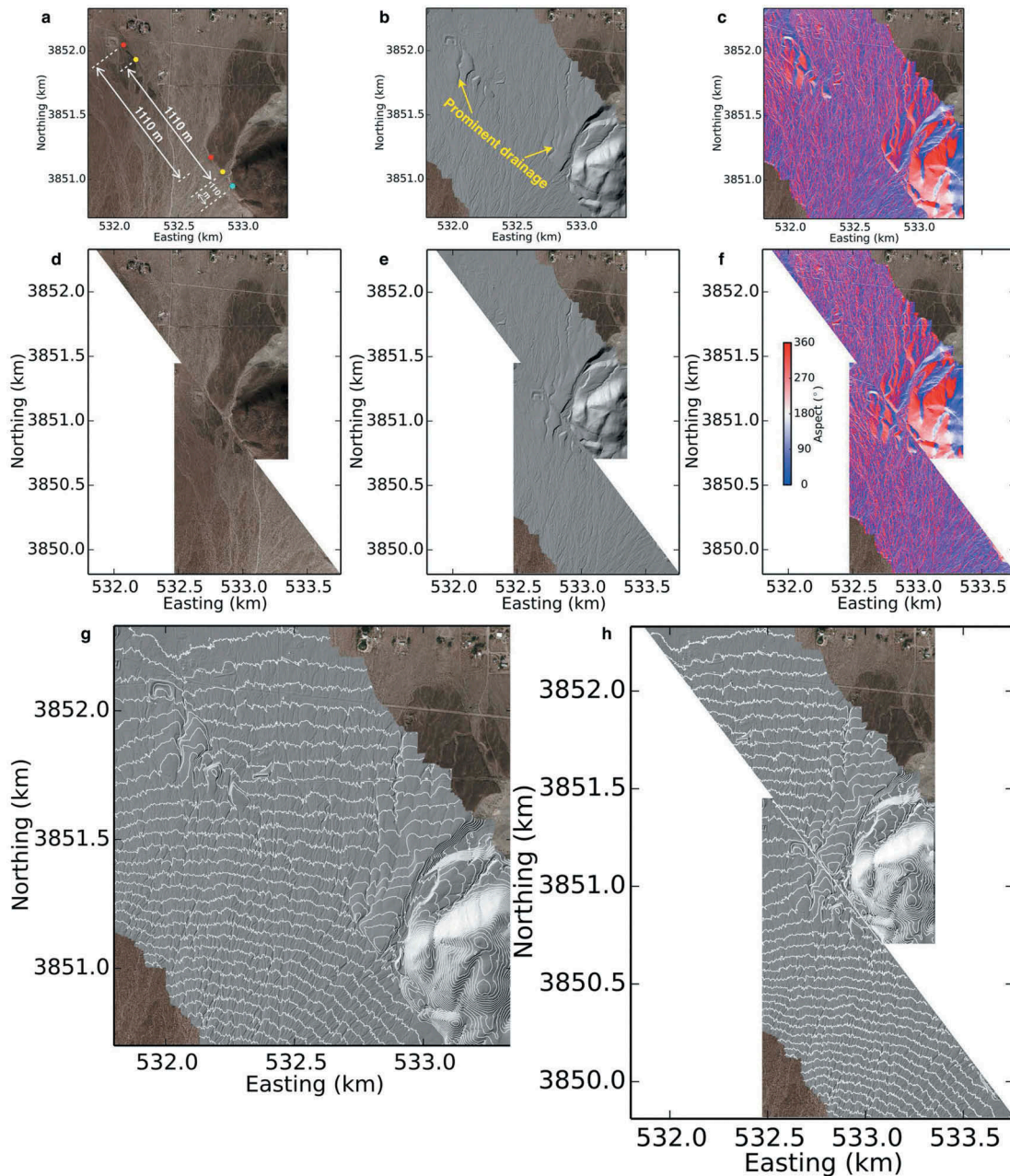
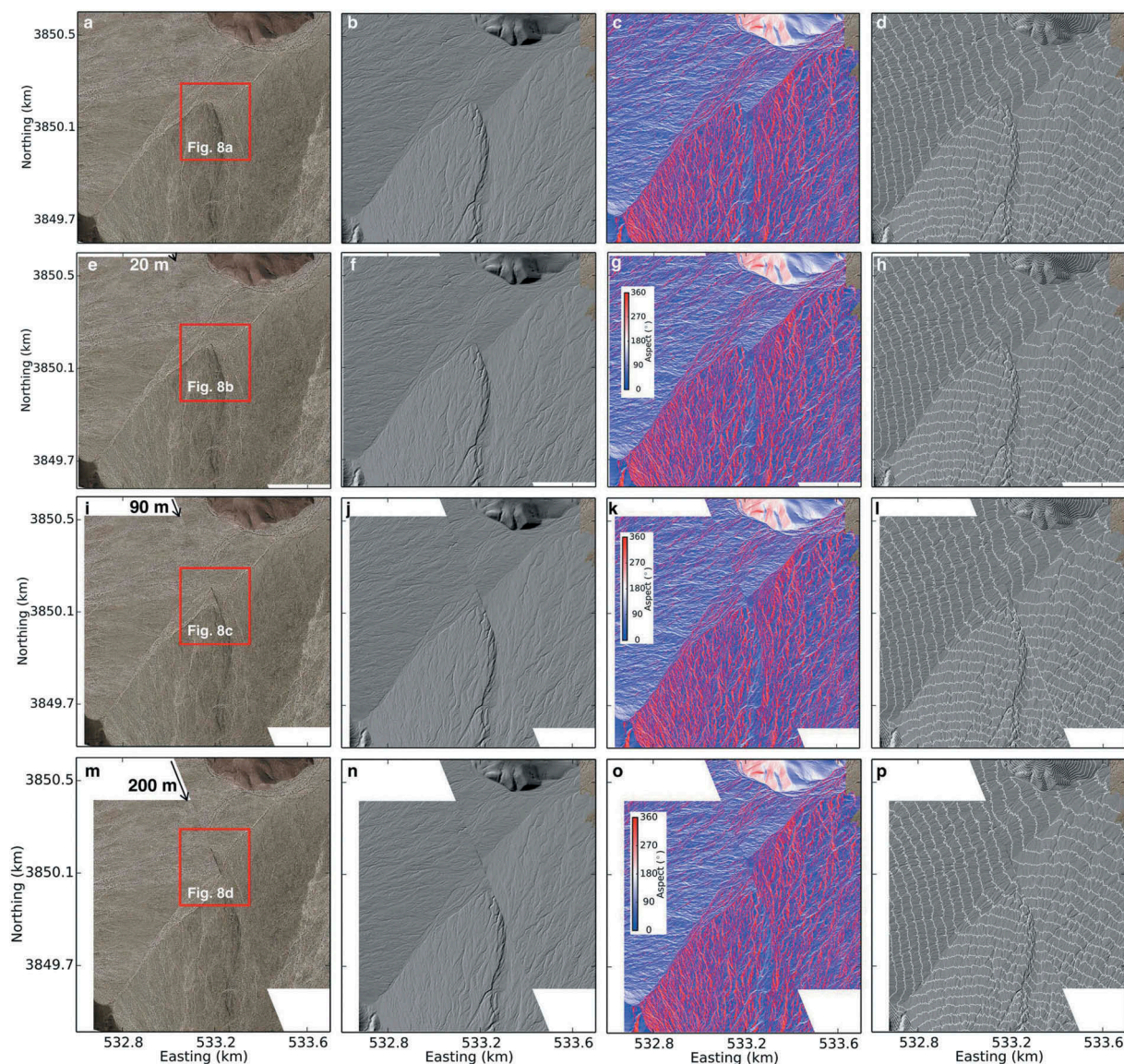**Figure 7.** Displacement of the TR alluvial fan (offset 2 outlined in Figure 3(b)). (a) Aerial image of the TR alluvial fan. (b) LiDAR hillshade overlain on aerial image. (c) Slope aspect derived from LiDAR DEM overlain on aerial image. (d) Elevation contour (white lines) overlain on the hillshade, contour interval is 2 m. (e–h) Restoration of 20 m displacement by aligning the TR-ASC boundary with an active channel on the northeastern wall of the Calico Fault (see dashed cyan line in Figure 8(a)). This assumes the boundary of the TR alluvial fan was originally highly nonlinear (Figure 8(a,b)). (i–l) Restoration of 90 m displacement when aligning linear downstream channel with oldest upstream fan edge, assuming the ASC incised completely into the IAF surface (Figure 8(g)). (m–p) Restoration of 200 m displacement assuming the anastomosing stream channel (ASC) surface incised completely into the TR alluvial fan (Figure 8(h)).

displacement. We note that the TR alluvial fan edge immediately southwest of the fault is smoothed by erosion, and the TR alluvial fan edge immediately northeast of the fault may have been reworked by a creek that runs close to the fault, or be partially buried by colluvium (Figure 8(a,b)).

Using the LaDiCaoz software, we derive a displacement estimate of 169 m by minimizing misfit between two elevation profiles along two sides of the fault trace (Figure 9). However, stream channels near the TR alluvial fan offset are not significantly deeper than surrounding surfaces, and elevations close to the fault may have been modified by desert flow of vertical motion. Thus, correlating elevation profiles with LaDiCaoz can result in an estimate with high uncertainty for this alluvial fan. The wide range of possible displacement estimates for the TR alluvial fan highlights the challenges in reconstructing the offset of a structurally complex and relatively young landform subjected to rapid reworking by desert flow.
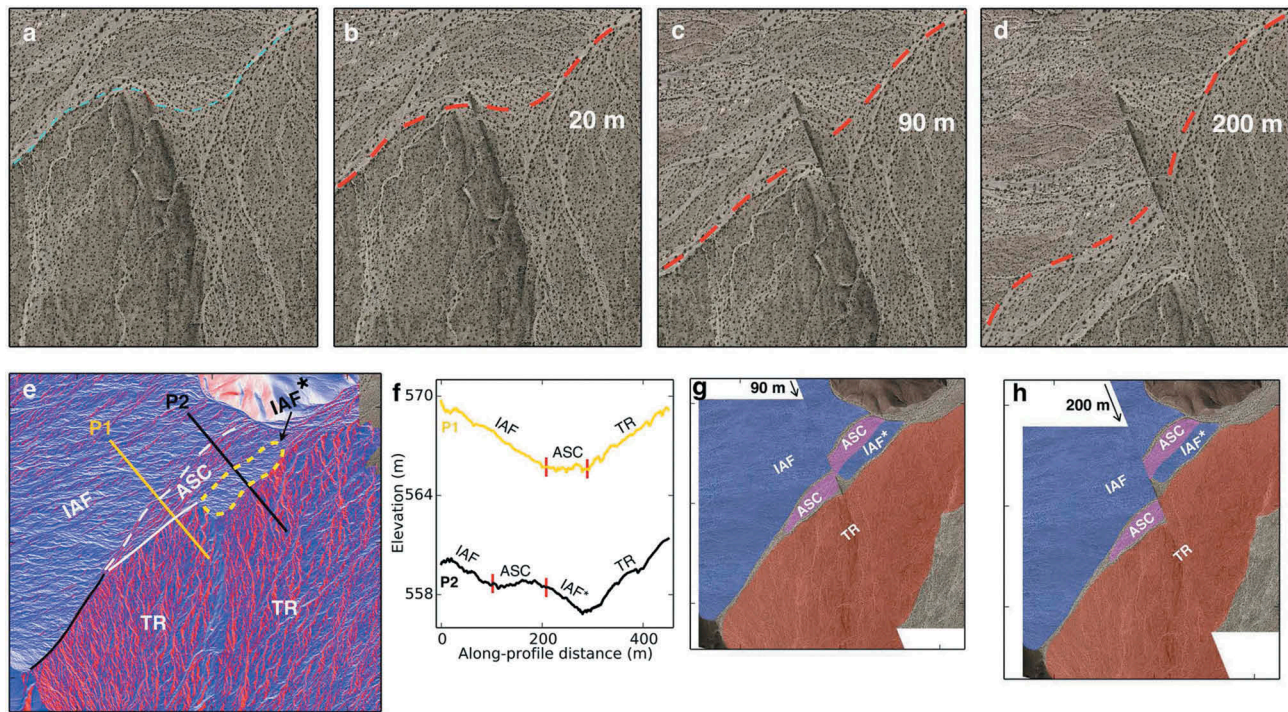
Figure 8. Different restorations of the offset at the TR alluvial fan. (a–d) Zoomed in images outlined by red boxes in Figure 7(a,e,i, m). Red line in (a) marks the 20 m displacement for the restoration in (b). (e) An enlarged slope aspect map of Figure 7(c), trends of palaeostream channels within the dashed shape (IAF*) are the same as the broader intermediate-aged alluvial fan surface (IAF). (f) Two elevation profiles marked by straight golden and black lines in (e). (g, h) show two different restorations with different units shaded.

4. New age estimates

Both the numerical dating and offset reconstruction can cause significant uncertainties in geologically derived fault slip rate estimates. Ideally, the offset feature to be dated would have formed over a short interval of time, sometime after fault initiation. Alluvial fans in the southwestern US, mainly represent Pleistocene and younger features, are thought to have formed in discrete intervals associated with climatic cycles/transition (e.g., McDonald *et al.* 2003; Dorn 2009; Miller *et al.* 2010; Shepard *et al.* 2018), and hence can be useful for estimating geological fault slip rates.

We used several independent techniques and cross-correlated the results to estimate the ages of our two alluvial fans. The degree of rubification (Fe oxide coating) or desert varnish (Fe-Mn oxide coating) on surface clasts, the development of desert pavement, and the presence or absence of a well-developed caliche horizon, serve as qualitative age indicators. By these measures, the ALR alluvial fan is clearly older than the TR alluvial fan. Quantitative techniques such as terrestrial cosmogenic nuclides (TCN) and optically stimulated luminescence (OSL) dating were also used in this study. Both qualitative and quantitative techniques are described below.

4.1. Desert pavement development

Alluvial fan surfaces vary in the ratio of aeolian fine sediments and stony pavement (desert pavement) with the percentage of stony pavement increasing with time. Wells *et al.* (1985) quantified this process for the northeast Mojave by estimating the percentage of stony pavement on a series of basalt flows of known age. Assuming similar processes apply to our area, the technique can be used to estimate a minimum age for a given alluvial fan surface (because of saturation effects the technique may not define an upper bound). Since the desert pavement is weak to moderately developed in the younger surfaces, we only analysed the ALR alluvial fan surface. We estimated the density of stony pavement on the ALR alluvial fan surface based on surface colour and correlation with exposed sand on four randomly selected photographs of the fan surface (Supplementary Figures S3–S6). Results suggest a minimum age of about 259 ka for the ALR alluvial fan (Figure 10(a)).

4.2. Carbonate rind thickness

Carbonate coatings on cobbles and boulders increase in thickness with increasing age. Amoroso (2006) developed a carbonate rind thickness model
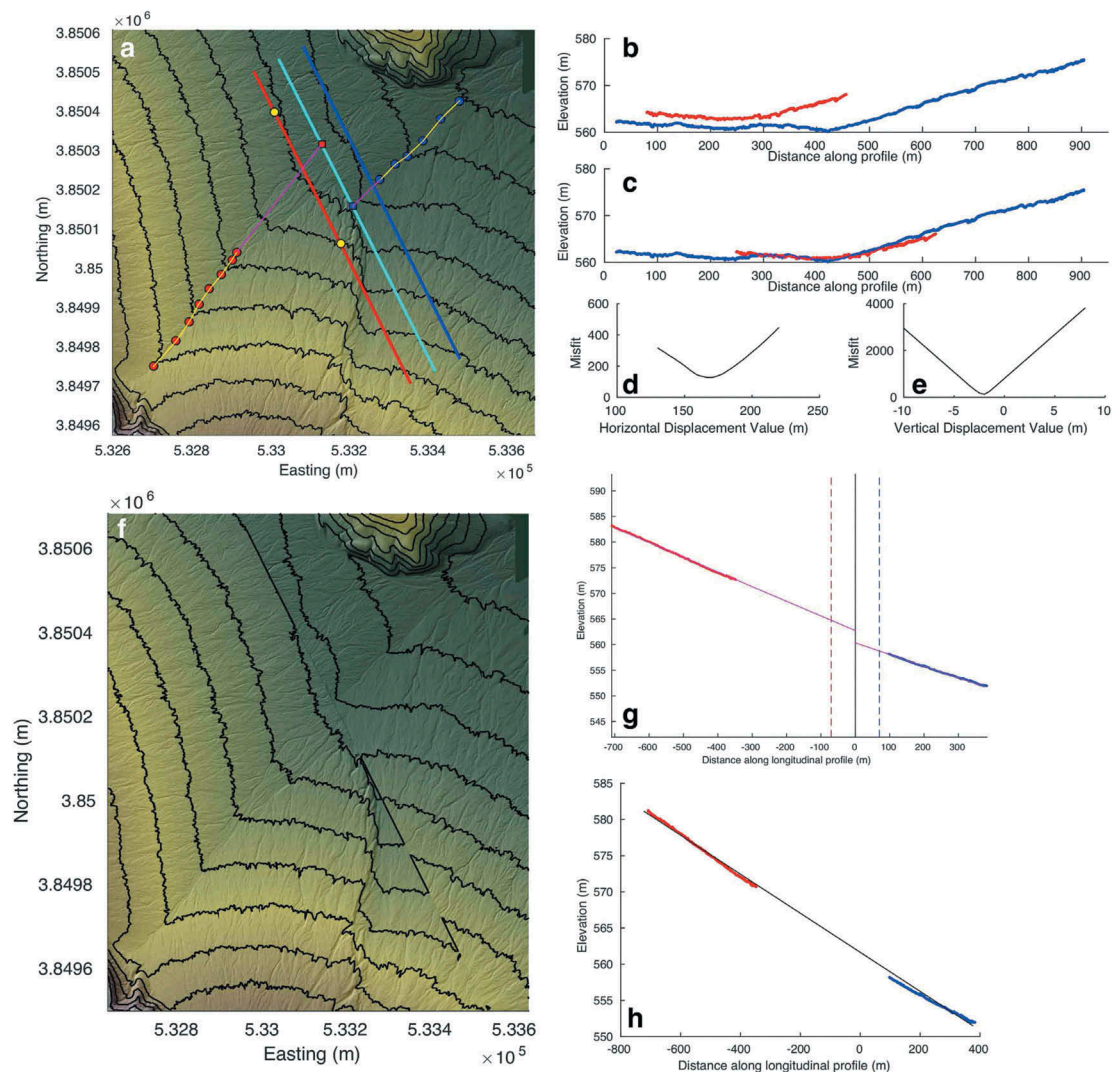
Figure 9. Displacement restoration using LaDiCaoz (Zielke *et al.* 2015; Haddon *et al.* 2016) for the TR alluvial fan. Markers in each subplot correspond to the same parameters described in Figure 6. Note that due to the complexity of the fan surfaces, we do not pick points near the fault to define the offset profiles, instead, we use the linear traces far from the fault to define an offset channel and extend them onto the fault. Displacement restoration from this fan is 169 m. Note that the reconstructed channel in (h) cannot be well fit by a straight line, probably due to uneven subsidence or erosion, or incorrect restoration since desert flow seems to have significantly modified the surface feature.

for the Mojave Desert, where rind thickness (in mm) is 0.0889 + 0.0079 × (surface age in ka). In principle, this model could be used to estimate an age for the ALR alluvial fan, which has well-developed coatings on cobbles and boulders (Supplementary Figure S2). However, a range of thicknesses is observed, leading to a rather wide range of age estimates, with a maximum of 482 ka for the ALR alluvial fan (Figure 10(b)). In addition, the model of Amoroso (2006) is only calibrated to ~130 ka, hence the accuracy for the ALR alluvial fan, which is likely much older, is not established.

4.3. Soil chronostratigraphy

Soil profile descriptions were performed in the field following standard techniques (Schoenegerger *et al.* 2012) (Supplementary Table S1). Profile development indices for observed profiles were calculated based on field observations following the method of Harden (1982). All of the profiles contained a ~10-cm-thick surface horizon with vesicular pores, secondary carbonates, and generally finer soil textures than underlying horizons indicating substantial contribution of fine grained aeolian material to surface horizons (Wells *et al.* 1985).

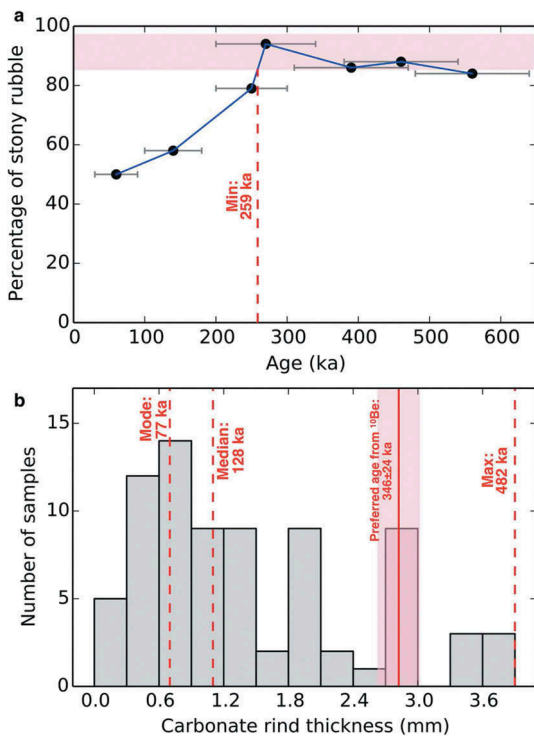**Figure 10.** Age constraints from stony rubble packing on the alluvial fan surface and carbonate rind thickness. (a) Percentages of pebble coverage for flow surface with different ages, reflecting degree of packing on the desert pavement. Black dots with error bar show data depicted in Wells *et al.* (1985), pink corresponds to the range of pebble coverage percentage for the ALR alluvial fan surface (86–97%, calculated using photos taken during our field investigation, see Supplementary Figures S3–S6). Dashed red line mark the corresponding age of the intercept between a piecewise model and the lower bound of pebble coverage. (b) Histogram of carbonate rind thickness for samples collected from evacuated pits and exposures rocks at a scarp. Thicknesses are measured under a ×10 binocular scope, using a stainless steel ruler with 1 mm scale (see example in Supplementary Figure S2). Dashed red lines mark the mode/median/max thickness, annotations are corresponding ages calculated using the model of Amoroso (2006). Solid red line marks calculated thickness based on the preferred age for ALR alluvial fan from [10]Be exposure dating, pink area marks the uncertainty.

The Calico-Pit2 profile in the TR alluvial fan exhibits minimal soil development in terms of pedogenic structure formation, reddening, and clay accumulation, with several lithologic discontinuities observed along with stratified sands and gravels in the subsurface. Subsurface horizons do contain secondary carbonates, mainly in the form of coatings on the bottom of gravels. The lack of pedogenic alteration resulted in a taxonomic classification of Typic Haplocambid (Soil Survey Staff 2014), and a profile development index value < 10 consistent with Holocene and latest Pleistocene (late marine isotope stage 2) aged soils observed in other areas of the Mojave (Harden *et al.* 1991).

The CalicoA and Calico-Pit3 profiles in the ALR alluvial fan exhibit greater degrees of soil development, with substantial reddening and secondary carbonate accumulation, and a near completely interlocked surface pavement. The soils classify as Typic Haplocalcids (Soil Survey Staff 2014), and profile development indices for these profiles ranged from ~18 to 25, with a greater degree of development in the CalicoA profile. These profile development indices are consistent with soils dated to ~200–250 ka in other Great Basin soil chronosequences (Harden *et al.* 1991). Field observation of the CalicoA profile suggested it may have been partially affected by erosion based on its soil morphologic features and location on the edge of the fan surface. Excavation of shallow pits in the centre of the ALR alluvial fan bodies indicated a depth of 35–40 cm to reach the top of the Bk2 horizon versus a depth of 28 cm in the sampled and described CalicoA profile, suggesting a potential loss of 7–12 cm of depth due to erosion. Including this additional depth in the calculation of the profile development index pushes the age correlation estimate close to 300 ka.

4.4. OSL dating

OSL dating determines the time elapsed since a sediment sample was last exposed to daylight (Aitken, 1998). The method relies on the interaction of ionizing radiation with electrons in semi-conducting minerals within buried sediment, which results in metastable accumulation of charge. Illumination of the sediment releases the charge as a measurable emission of photons (luminescence). The methods assume that mineral grains during or immediately prior to the transport were exposed to daylight to set them to their geological zero residual level. Upon burial, daylight exposure ceases and essentially the luminescence signal begins to accumulate due to radiation arising from the decay of ambient radio-isotopes that include U, Th, Rb, and K, and from cosmic rays. Given that, as a first approximation, the radiation exposure (the dose rate D_R) is constant over the timescales of interest, luminescence builds up (equivalent dose D_E) in the minerals in proportion to the duration of burial and the concentration of radioisotopes in the sample environment and the cosmic dose. The depositional age (A) of the sample is thus a ratio of luminescence acquired and the rate of luminescence acquisition, that is, $A = D_E/D_R$ (Aitken, 1998; Murray and Olley 2002; Singhvi and Porat 2008).

Since the age of the ALR alluvial fan is likely to be beyond the range of applicability for the OSL technique, we only sampled the TR alluvial body, at the Calico-Pit2 (location shown in Figure 3(b)). Three OSL

samples were collected at 75, 55, and 33 cm of depth (Calico F1, Calico F2, and Calico F3, respectively) by hammering 15-cm-long, 5-cm diameter plastic tubes into the sediment (Supplementary Figure S7). Detailed descriptions of the OSL sample processing steps are given in Supplementary Text S1.

Table 1 presents the radioisotope, water content, and cosmic dose, D_R, D_E, and OSL age for the samples. OSL characteristics and age determination are also discussed in more detail in Supplementary Text S1, Figures S8 and S9. The OSL ages range from 5.0 ± 0.4 ka (shallow sample) to 5.8 ± 0.4 ka (deep sample).

4.5. TCN [10]Be surface exposure dating

Cosmic rays generate terrestrial cosmogenic nuclides (TCNs) in Earth's atmosphere and surface that are produced at a known rate and can be used to date a variety of materials and processes. For alluvial fan surfaces, it is useful to focus on techniques where the nuclides are produced *in situ*, a technique known as TCN surface exposure dating. Since quartz is a common rock-forming mineral rich in oxygen, a spallation reaction that transforms ^{16}O to ^{10}Be (1.4×10^6 years) is especially useful (Gosse and Phillips 2001). Comparison of surface samples to depth profiles can be helpful in establishing the degree of inheritance of ^{10}Be, which otherwise can lead to anomalously old age estimates (alluvial fans often develop by re-mobilizing older alluvial material, and inheritance is a particular problem for younger fans, where the majority of the ^{10}Be signal can be inherited). Overland sheet flow, erosion, and bioturbation can also disturb surface boulders, leading to anomalously young ages. Older alluvial fans are more likely to experience such disturbance.

We collected rock samples (>150 g each) from surface boulders and cobbles on the ALR and TR alluvial fan surfaces (red dots in Figure 3(b)). Sediment samples for depth profiles were collected at depth intervals of ~30 cm for 3 pits to a depth of 2 m: CalicoA and Calico-Pit3 for the ALR alluvial fan, and Calico-Pit2 for the TR alluvial fan (light blue squares in Figure 3(b)). Supplementary Figure S10 shows pictures of collected samples. Both types of sampling were used for TCN dating using ^{10}Be. Rock samples were chosen following criteria described in Gray *et al.* (2014), Frankel *et al.* (2015), and Hedrick *et al.* (2017), including: (1) large size, typically >50 cm in length; (2) stable boulders inset into the ground; (3) little sign of erosion; and (4) quartz rich lithology. If boulders were absent whole cobbles were collected. The highest positions on alluvial fan surfaces were selected for depth profile trenches to minimize the possibility of surface erosion.

Table 1. Summary of OSL dating results from extracted from sediment, sample locations, radioisotopes concentrations, moisture contents, total dose-rates, D_E estimates, and optical ages.

Sample number	Location (°N/°W)	Altitude (m asl)	Depth (cm)	U[a] (ppm)	Th[a] (ppm)	K[a] (%)	Rb[a] (ppm)	Cosmic dose[b,c] (Gy/ka)	Total dose-rate[b,d] (Gy/ka)	n[e]	n[f]	Dispersion D_E (%)	Average equivalent dose[g,h] (Gy)	Average equivalent dose[g,i] (Gy)	OSL Age[g,h] (ka)	OSL Age[g,i] (ka)
Calico F1	34.7925/116.6371	596	75	2.5	14.5	2.8	110	0.21 ± 0.02	4.40 ± 0.24	24	15	19	25.42 ± 1.07	25.46 ± 1.0	5.8 ± 0.4	5.8 ± 0.4
Calico F2	34.7925/116.6371	596	55	2.1	14.1	3.0	118	0.22 ± 0.02	4.45 ± 0.25	24	13	21	27.66 ± 1.03	23.27 ± 2.7	6.2 ± 0.4	5.2 ± 0.7
Calico F3	34.7925/116.6371	596	33	2.3	14.9	3.1	120	0.22 ± 0.02	4.73 ± 0.26	32	15	40	29.98 ± 1.31	23.84 ± 1.5	6.3 ± 0.4	5.0 ± 0.4

[a]Elemental concentrations from NAA of whole sediment measured at Activation Laboratories Limited Ancaster, Ontario Canada. Uncertainty taken as ±10%.
[b]Estimated fractional day water content for whole sediment is taken as 10% and with an uncertainty of ±5%.
[c]Estimated contribution to dose-rate from cosmic rays calculated according to Prescott and Hutton (1994). Uncertainty taken as ±10%.
[d]Total dose-rate from beta, gamma, and cosmic components. Beta attenuation factors for U, Th and K compositions incorporating grain size factors from Mejdahl (1979). Beta attenuation factor for Rb is taken as 0.75 (cf. Adamiec and Aitken 1998). Factors utilized to convert elemental concentrations to beta and gamma dose-rates from Adamiec and Aitken (1998) and beta and gamma components attenuated for moisture content. Dose-rates calculated through Aberystwyth University DRAC calculator (Duncan et al. 2015).
[e]Total number of single-aliquot measured.
[f]Number of replicated equivalent dose (D_E) successfully measured determined from replicated single-aliquot regenerative-dose method (SAR; Murray and Wintle 2000). These are based on recuperation error of <10%.
[g]Weighted mean and standard error equivalent dose (D_E) for all aliquots. The uncertainty includes an uncertainty from beta source estimated of ±5%.
[h]Uncertainty incorporate all random and systematic errors, including dose rates errors and uncertainty for the D_E.
[i]Mean and standard error equivalent dose (D_E) for minimum peak. If D_E dispersion was >20%, then a 2 mixing model was considered. The uncertainty includes an uncertainty from beta source estimated of ±5%.

All rock samples were prepared with standard procedures, including crushing, magnetic separation, heavy-liquid mineral separation (only for samples with significant heavy minerals or feldspars), etching, dissolution, purification, and target loading. Sediment samples went through the same processing procedures except for crushing: we sieved sand grain sizes between 0.25 and 0.5 mm before subjecting them to the procedures described above. Sand samples from Calico-Pit2 and Calico-Pit3 profiles did not yield a sufficient quantity of quartz, thus in order to increase the amount, small quartz-rich pebbles were added, with sizes between 0.5 and 12.5 mm; these pebbles were crushed, later sieved, and added to the sand quartz fraction of 0.25–0.5 mm. Detailed descriptions of these samples and the TCN sample processing steps are given in Text S2 of the Supplement. Uncertainties for all ages are estimated at 2σ (95% confidence interval).

4.5.1. ALR alluvial fan

Ten rock samples on the ALR alluvial fan surface yield ages that range from ~75 to 346 ka (Figure 11 and Supplementary Table S2). Eight have ages of ~100 ka, while the other two (erosionally resistant quartz samples) have ages that are >300 ka.

To better constrain results and assess possible inheritance and erosion effects, depth profiles with samples collected at various depths from two trenches were used to help assess the validity of the surface exposure ages: one trench (CalicoA) at the southern corner of the main body of ALR alluvial fan, and a second one (Calico-Pit3) at the small fan surface to the northwest. Ideally, an exponential decrease of TCN concentration with depth is expected if the alluvial fan formed in a simple way, with no disturbance since formation and with all sediments that later became part of the alluvial fan containing the same concentration of inherited TCNs as that of the initial alluvial fan formation. The concentration of ^{10}Be versus depth profile thus contains information on exposure age, erosion history and inheritance. Figure 12(a) shows the ^{10}Be concentration versus depth profile for CalicoA, with the expected trend (decreasing ^{10}Be with depth).

A Bayesian-Monte Carlo simulation allows simultaneous estimation of age, erosion history, and inheritance (Hidy *et al.* 2010; Hidy 2013). Loose constraints are applied, with age, erosion and inheritance allowed to vary between conservative high and low values, and Monte Carlo techniques are used to derive best estimates of the model parameters. The allowed ranges of the constraints used here are: 0–1200 ka for exposure age, 0–0.5 cm/ka for erosion rate, and 0–1.3 × 10^5 atoms/g for inheritance. No shielding was applied for the simulation (all samples were located far from high-relief features, and the environment is not currently favourable for snow cover). We assume an attenuation length of 160 ± 5 g/cm^2

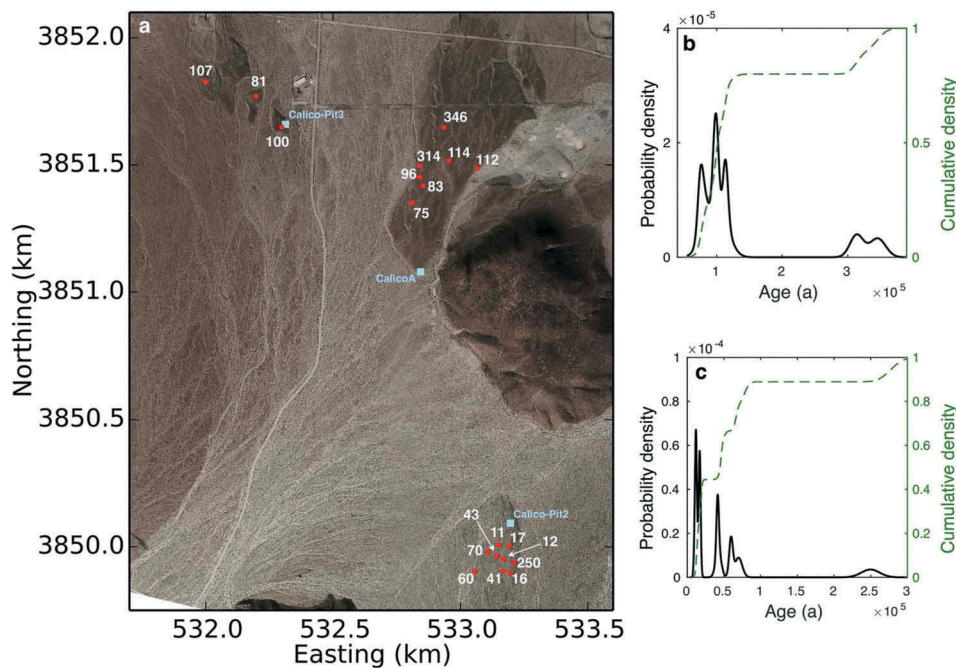**Figure 11.** TCN ^{10}Be ages (ka; see Table 2 for the age uncertainties) of rock samples collected on alluvial fan surfaces. (a) Red dots show locations of rock samples. Their apparent ages are shown in adjacent white annotations. (b) Age probability density function (PDF) of rock samples on the ALR alluvial fan, derived by using the program of Zechar and Frankel (2009). (c) Age PDF of rock samples on the TR alluvial fan.
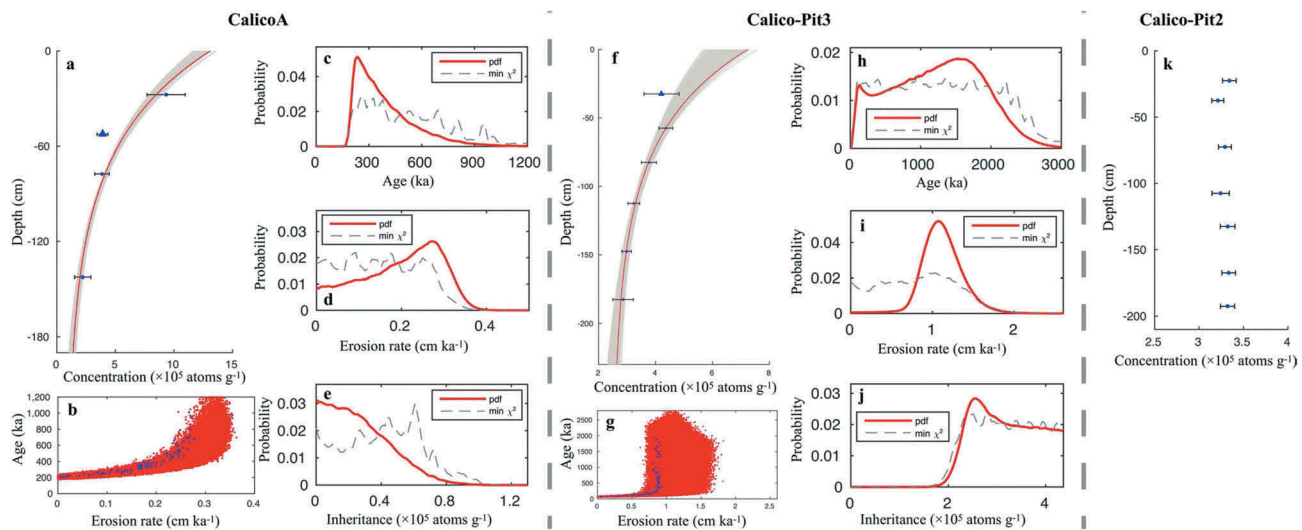
Figure 12. [10]Be versus depth, and corresponding Bayesian-Monte Carlo simulations. (a) through (e) show results for profile CalicoA. In (a), blue markers with error bar show measured [10]Be concentration of samples, grey curves are from 100,000 Bayesian-Monte Carlo simulations following Hidy et al. (2010) and Hidy (2013), red curve shows best fit. (b) shows age versus erosion rate, each red dot represents one possible solution, the scatter defines the solution space. Blue dots mark the top 100 fits (lowest chi-square). Red lines in (c–e) show the age probability density functions (PDF) of age, erosion rate, and inheritance from the simulation, dashed black lines shows relative value of the minimum chi-square. Note that one sample collected at 50 cm depth for CalicoA (marked by blue triangle in (a)) was not used because its concentration lies well off the exponential trend. Inclusion of this sample yields a higher erosion rate and inheritance, and a lower minimum age. (f–j) Corresponding Bayesian-Monte Carlo simulations for profile Calico-Pit3. Sample at 30 cm depth (blue triangle in (f)) was excluded from the simulations as it lies well off the expected exponential trend. Because a conservative criterion for this depth profile would yield unrealistically high end-members of inheritance, we used the maximum [10]Be concentration among the six samples to define the upper limit of the inheritance for the simulations. (k) Sample depth versus [10]Be concentration for Calico-Pit2 trench in the TR alluvial fan. Lack of exponential decrease with depth suggests that this fan has undergone complex deposition-erosion history. Note for CalicoA, error bars in (a) show 5σ confidence level. This was necessary to run the simulator due to the data scatter (see also Hedrick et al. (2017)). Error bars in (f) and (k) show 2σ confidence level.

and a stochastic uniform density of 1.9–2.5 g/cm³, consistent with previous studies in similar environment (e.g. Hidy et al. 2010; Owen et al. 2011a; and Gray et al. 2014). We then estimate the probability density functions for exposure age, erosion rate, and inheritance (Figure 12(a–e)). The most probable Bayesian age for CalicoA is 222 ka. However, without tight constraints on the other two parameters, the age estimate has a broad distribution, with a 2σ range between 196 and 832 ka (Figure 12(c), note tail on the upper bound is significantly longer). The 2σ upper limit of inheritance is 7.06×10^4 atoms/g, equivalent to an age of ~15 ka.

We applied the same method to the depth profile of Calico-Pit3, with constraint ranges as follows: 0–3000 ka for exposure age, 0–2.6 cm/ka for erosion rate, and 0–4.4×10^5 atoms/g for inheritance (a conservative high will produce unrealistically high inheritance, thus the maximum [10]Be concentration among the 6 samples was used as high-end constraint). The result gives a wide age distribution, with 2σ range between 99 and 2401 ka. Note that the most probable erosion rates from two depth profiles are smaller than the 3.05 ± 0.62 cm/ka erosion rate estimated at the Calico

Archaeological site, ~19 km away from our study area (Owen et al. 2011a). Assuming the same erosion rate as Owen et al. (2011a) yields a poor fit to the depth profiles and unrealistically old exposure ages. Due to the detailed soil profile analysis conducted, we recognize at CalicoA that the upper section of the surface was eroded about 7–12 cm (Section 4.3). Adjusting the depths for samples in the depth profiles by adding a 10 cm depth results in a slightly lower erosion rate that balances the depth adjustment, but the age and inheritance are essentially the same. While imperfect knowledge about erosion over the lifetime of the alluvial fan surface can limit the precision of the age estimates from depth profiles, these age limits allow us to exclude some rock samples from further study. For examples, rock samples with apparent ages of ~100 ka or less are clearly not representative, perhaps due to incomplete exposure (partial burial) or outer surfaces that may have been eroded.

Two erosionally resistant quartz samples yield apparent ages of >300 ka. We use the apparent age of the oldest sample (346 ± 24 ka) as the most reliable estimate of the exposure age for the ALR alluvial fan

surface. The depth profile results suggest that inheritance would not change this age significantly. This age estimate is consistent with results from the carbonate rind thickness, desert pavement density, and soil chronostratigraphy techniques (Figure 13(a)).

4.5.2. TR alluvial fan

Among 9 dated rock samples collected on the TR alluvial fan surface, one (Calico-6) has an age of 250 ka. This age is incompatible with the observed soil development here (no visually obvious rubification and carbonate coating). Inheritance from older units likely explains this anomalously old age. The remaining eight samples still exhibit a wide range of ages, from 10.9 to 70 ka (Figure 11). The depth profile for this fan, Calico-Pit2 does not show the expected exponential decrease in ^{10}Be concentrations with depth (Figure 12 (k)), indicating inheritance saturation. The OSL samples provided ages in the range of 5.0 ± 0.4 to 5.8 ± 0.4 ka for the upper metre of the fan deposit, suggesting a Holocene age for this fan surface and indicating the fan sediments were deposited in a relative short period of time. The young age and relatively fast sedimentation indicated by the OSL results, combined with inheritance saturation of ^{10}Be in depth profile, presumably explains the lack of exponential decrease with depth of the ^{10}Be concentrations.

For TCN dating techniques, understanding and quantifying inheritance is important. This is especially true for younger deposits and surfaces which can cannibalize older fan material and have not had sufficient time to generate a unique age signature. We estimated an inheritance of ~60 ka from our Calico-Pit2 depth profile. However, most of the rock samples from the TR alluvial fan have young apparent ages that are incompatible with inheritance saturation, indicating

that inheritance in boulders and sand can vary significantly.

All of our TCN dated boulders are much older than the OSL results. There are two possibilities to explain the TCN results for the TR alluvial fan: (1) The true exposure age of the TR alluvial fan is closest to the young cluster (10.9–17.1 ka) of apparent ages from rock samples with inheritance subtracted. The other rock samples have larger amounts of inheritance, and the depth profile represents an average inheritance for the fan material; (2) The true exposure age is significantly older than the young cluster of apparent ages. In this case, a complex formation-exposure history has occurred, such that the depth profile does not show the expected exponential decrease in ^{10}Be concentrations with depth. The first possibility agrees with the soil development and OSL dating results. The second possibility requires that the youngest four samples have experienced significant erosion or shielding after fan formation, which we think is unlikely given its relatively young age based on lack of rubification and desert pavement development.

We thus favour the first explanation. In this case, inheritance estimated from the depth profile (equal to ~60 ka) does not equal the inheritance of most of the rock samples (<45 ka). Since the scatter of apparent ages is largely determined by inheritance, we therefore discard the older apparent ages. Based on the four boulders with youngest apparent ages we estimate the weighted mean and 2σ, and obtain 14.0 ± 5.8 ka. Note this is still a maximum age estimate for the TR alluvial fan as it contains unknown amount of inheritance. If the OSL dated age of ~5 ka represents the true age, then inheritance accounts for ~9 ka among the youngest cluster of ages. Dating sediments in the Mojave through OSL can be also challenging, OSL

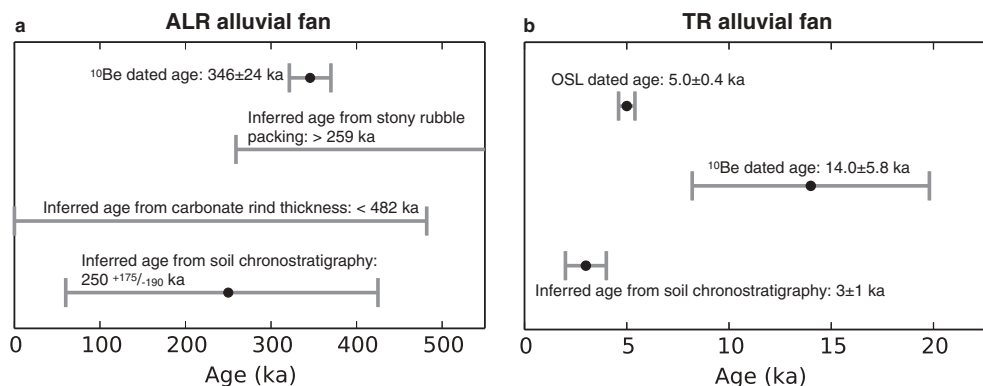**Figure 13.** Age constraints for the ALR and TR alluvial fan. (a) ^{10}Be dated age of 345±24 ka is our preferred age estimate for the ALR alluvial fan. Degree of desert pavement packing, carbonate rind thickness and soil chronostratigraphy give additional constraints on the fan age. (b) The youngest OSL dated age is a minimum age for the TR alluvial fan, and the ^{10}Be dated contains an unknown amount of inheritance.

measurements may give ages that are too young, for example, due to low OSL sensitivity, poor quartz characteristics, high dose rates, and low water estimates (e.g. Owen *et al*. 2007; Lawson *et al*. 2012), 5 ka may therefore represent as a minimum age for the TR alluvial fan.

These results suggest a young age for the TR alluvial fan, consistent with proposed ages for regional alluvial fan generation by Miller *et al*. (2010), and consistent with soil chronology at this site (Figure 13).

5. Slip rate estimates

For the ALR alluvial fan, the displacement of 1110 ± 110 m and the TCN exposure age from the sample with the largest apparent age (346 ± 24 ka) yields a slip rate of 3.2 ± 0.4 mm/yr. For the TR alluvial fan, the OSL dating yields a minimum age of 5.0 ± 0.4 ka, and the TCN surface exposure dating gives a maximum estimate of 14.0 ± 5.8 ka. Displacement estimates of the TR alluvial fan are highly uncertain, hence the slip rate is not well constrained by our data (Figure 14). While a displacement estimate of 20 m, and the OSL age of 5 ka define a slip rate similar to the ALR alluvial fan data, the complex offset geometry and spread of geochronology data for this alluvial fan allow alternate interpretations. For example, the displacement estimate of 90 m and TCN

Figure 14. Plausible displacement for the TR alluvial fan offset. Dashed blue lines mark the minimum and maximum possible ages from OSL and TCN [10]Be dating. Red lines show the minimum and maximum possible slip rates for the Calico Fault (Sauber *et al*. 1994; Oskin *et al*. 2007a; McGill *et al*. 2015; Selander 2015). Grey area represents the range of plausible displacement for the TR alluvial fan offset, between 7 and 168 m. Black dots with error bars mark different restorations in this study.

exposure age of 14.0 ± 5.8 ka define a faster slip rate, 6.4 ± 2.7 mm/yr; the same displacement but using the OSL dated age results in an even higher slip rate. In the discussion below, we use the slip rate estimate based on data from the ALR alluvial fan as the best estimate for the long-term average (several hundred thousand year) slip rate of the Calico Fault.

6. Discussion

Our new slip rate estimate of 3.2 ± 0.4 mm/yr based on the ALR alluvial fan data is considerably faster than previously published values for the Calico Fault (Table 2). This new slip rate is faster than the estimate of 1.8 ± 0.3 mm/yr from the 56.4 ± 7.7 ka old 'K' alluvial fan of Oskin *et al*. (2007a), more than double the slip rate estimate of 1.4 ± 0.4 mm/yr from the 650 ± 100 ka old 'B' alluvial fan by Oskin *et al*. (2007a), and more than double the 1.4 $^{+0.8}_{-0.4}$ mm/yr estimate from a 17.1 $^{+1.6}_{-2.6}$ ka 'Q2c' unit southwest of the Rodman Mountains reported by Selander (2015). Although our estimate may represent a maximum slip rate due to limited knowledge of the erosion history and corresponding uncertainty in the alluvial fan age (i.e. the alluvial fan could be older), the lower slip rate limit should not be much lower, for three reasons: (1) the probability density function (pdf) of the age–depth profile CalicoA (Figure 12(c)) skews strongly to ~300 ka, with a correspondingly small probability for ages >600 ka; (2) a slip rate of 1.8 mm/yr for the ALR alluvial fan requires that its exposure age would be >600 ka given the 1110 m displacement, incompatible with the carbonate rind thickness and soil development data, which require an age much younger than this; and (3) our displacement and age estimates for the TR alluvial fan, while they have larger uncertainties, also allow a faster rate interpretation (though it does not require it; Figure 14). For example, assuming the smallest possible displacement (20 m) and the OSL results (5.0 ± 0.4 ka) gives a rate of ~4 mm/yr. Any of the larger displacement estimates requires a correspondingly faster rate if the OSL age estimate is correct.

Since the various published rate estimates and our own estimates are based on offsets from different locations along the Calico Fault and features with a range of ages, there are several possible explanations for the differences, including: (1) the slip rate on the Calico Fault changes along strike; (2) the slip rate on the Calico Fault changes with time; (3) one or more of the assumptions used to estimate slip rates are in error; and/or (4) all of the data are correct in a strict sense but the estimates represent on-fault slip rates at the corresponding sites. In this case the fastest one may be
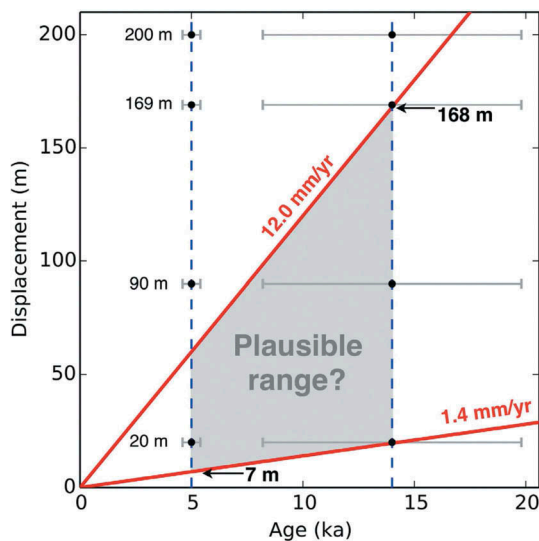
Table 2. Displacement, age, and slip estimates from Oskin *et al.* (2007a, 2007b), Selander (2015), and this study.

Surface	Sample	Dating technique	Age (ka)	Age uncertainty (ka, 2σ)	Preferred rate [a] (mm/yr, 2σ)
ALR (this study) Displacement (2σ): 1110±110 m	Calico-9	^{10}Be	345.7	24.3	3.2 ± 0.4
	Calico-11	^{10}Be	313.7	20.4	
	Calico-12	^{10}Be	75.3	8.3	
	CA-14	^{10}Be	113.6	7.5	
	Calico-20	^{10}Be	112.1	25.4	
	Calico-23	^{10}Be	81.5	23.2	
	Calico-25	^{10}Be	107	19.5	
	CA-104	^{10}Be	100.2	7.2	
	CA-106	^{10}Be	82.8	13.3	
	CA-107	^{10}Be	96.5	7.5	
TR (this study) Displacement: 90 m (note there are other possibilities, see Figures 7–9 and 14)	Calico-3	^{10}Be	41.4	3.3	6.4 ± 2.7
	Calico-7	^{10}Be	42.5	7.8	
	Calico-8	^{10}Be	59.6	5.1	
	CA-102	^{10}Be	70.4	9.9	
	Calico-1	^{10}Be	17.1	2.3	
	Calico-2	^{10}Be	12.1	2.2	
	Calico-5	^{10}Be	15.9	3.9	
	Calico-6	^{10}Be	249.7	24.9	
	CA-101	^{10}Be	10.9	2.8	
	Calico F1	OSL	5.8	0.4	
	Calico F2	OSL	5.2	0.7	
	Calico F3	OSL	5.0	0.4	
SWRM (Selander 2015) Displacement (2σ): 24^{+9}/$_{-10}$ m	Q2c depth profile	^{10}Be	17.1	$^{+1.6}$/$_{-2.6}$	1.4$^{+0.8}$/$_{-0.4}$
B (Oskin *et al.* 2007a, 2007b) Displacement (2σ): 900 ± 200 m	CC04-004-A	^{40}Ar/^{39}Ar	13966	4246	1.4 ± 0.4
	CC04-004-B	^{40}Ar/^{39}Ar	906	46	
	CC04-004-C	^{40}Ar/^{39}Ar	778	6	
	CC04-004-D	^{40}Ar/^{39}Ar	759	6	
	CC04-004-E	^{40}Ar/^{39}Ar	722	28	
	CC04-002-A	^{40}Ar/^{39}Ar	2234	676	
	CC04-002-B	^{40}Ar/^{39}Ar	907	116	
	CC04-002-C	^{40}Ar/^{39}Ar	776	46	
	CC04-002-D	^{40}Ar/^{39}Ar	756	18	
	CC04-002-E	^{40}Ar/^{39}Ar	763	16	
	CC04-002-F	^{40}Ar/^{39}Ar	777	52	
	CC04-002-G	^{40}Ar/^{39}Ar	4044	598	
	CC04-021	^{3}He	653.4	19.8	
	CC04-022	^{3}He	218.7	6.7	
	CC04-027	^{3}He	418.9	12.6	
	CC04-028	^{3}He	144	4.4	
	CC04-024	^{10}Be	73.5	1.9	
	CC04-025	^{10}Be	59.4	1.6	
K (Oskin *et al.* 2007a) Displacement (2σ): 100 ± 10 m	CC04-005	^{3}He	130.2	4.1	1.8 ± 0.3
	CC04-006	^{3}He	106.8	3.2	
	CC04-007	^{3}He	106.8	3.2	
	CC04-009	^{3}He	155.5	4.7	
	CC04-010	^{3}He	268.5	8.1	
	CC04-015	^{3}He	95.0	3.2	
	CC04-018	^{3}He	137.9	4.6	
	CC04-011	^{10}Be	57.1	1.5	
	CC04-012	^{10}Be	63.3	1.7	
	CC04-013	^{10}Be	57.6	2.0	
	CC04-014	^{10}Be	55.9	1.5	
	CC04-016	^{10}Be	53.4	1.4	
	CC04-017	^{10}Be	56.3	2.0	
	CC04-019	^{10}Be	48.3	1.3	
	CC04-020	^{10}Be	63.3	1.9	

[a]Slip rate estimate from ALR fan data is based on the reconstructed displacement of 1110±110 m and the age of an erosion resistant quartz sample Calico-9 (346±24 ka). Slip rate estimate from the TR alluvial fan is based on the displacement estimate of 90 m and weighted mean age of 14.0±5.8 ka (using two standard deviations as uncertainty) from TCN dating of four rock samples with apparent ages between 10.7 and 17.1 ka. Using OSL dating ages result in higher rates. Slip rate estimate by Selander (2015) is based on a depth profile Q2c at the southwest Rodman Mountains (SWRM), with a displacement estimate of 24^{+9}/$_{-10}$ m and an age estimate of 17.1$^{+1.6}$/$_{-2.6}$ ka. Slip rate estimate of B fan by Oskin *et al.* (2007a, 2007b) is from an assigned age of 650 ± 100 ka based on age data (see details in Oskin *et al.* (2007a) and a displacement estimate of 900 ± 200 m. Slip rate estimate of K fan by Oskin *et al.* (2007a) is from a displacement estimate of 110 ± 10 m and a mean average age of 56.4 ± 7.7 ka (inheritance estimate from active wash samples subtracted) based on ^{10}Be exposure age dating of rock samples.

closest to the true slip rate due to different amounts of slip localization and off-fault deformation.

Regarding a change in slip rate along strike (our first explanation), Oskin *et al*. (2007a) and Selander (2015) suggest that slip in the Calico-Blackwater Fault system varies spatially, with slip transferring from the Calico Fault to the Harper Lake and Blackwater faults via a set of thrust ramps or absorbed by folding adjacent to the Calico Fault. The two studies referenced above are separated by only ~8 km and have rates that differ by ~30%. Our study area is ~7 km from the study area of Oskin *et al*. (2007a), and ~15 km from the study area of Selander (2015) (Figure 15). To support an increase from 1.4 or 1.8 to 3.2 mm/yr would require that nearby faults (the fastest one is Camp Rock Fault, with slip rate ≤ 1.4 mm/yr (Oskin *et al*. 2008)) transfer almost all their slip to the Calico Fault within 15 km. While it seems overly complicated, we cannot preclude this possibility considering the highly discontinuous and complex nature of the Mojave section of the ECSZ. More studies are needed to explore the possibility of slip rate transfer along strike, or communication among nearby faults.

As for a change in slip rate over time (our second explanation), the displacement of the ALR alluvial fan
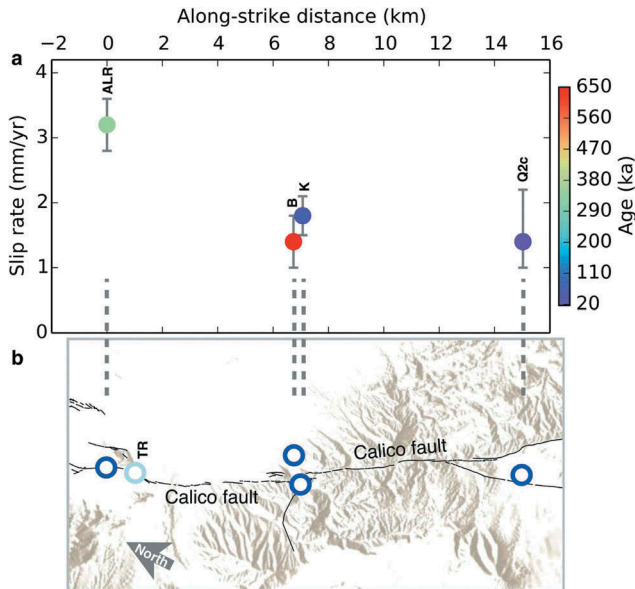

Figure 15. Along-strike slip rate estimates on the Calico Fault. (a) Colour represents age. ALR: 3.2 ± 0.4 mm/yr from this study; B: 1.4±0.4 mm/yr from the 'B' alluvial fan in Oskin *et al*. (2007a); K: 1.8±0.3 mm/yr from the 'K' alluvial fan in Oskin *et al*. (2007a); Q2c: 1.4 $^{+0.8}/_{-0.4}$ mm/yr from the 'Q2c' depth profile in Selander (2015). (b) Fault map shows the area outlined by dashed magenta box in Figure 1. Blue circles mark the geologic sites corresponding to (a). Light blue circle shows location of the TR alluvial fan. Black lines show major fault traces from U.S. Geological Survey and California Geological Survey (2006).

(1110 ± 110 m) is slightly larger than the 'B' alluvial fan (900 ± 200 m, with a surface exposure age estimate of 650 ± 100 ka) of Oskin *et al*. (2007a). To reconcile the displacement and age data, the Calico Fault would need to be inactive between the formation time of the 'B' alluvial fan and the formation time of the ALR alluvial fan. Unless the ALR alluvial fan has an exposure age similar as the 'B' fan, this seems unlikely, based on the age constraints described earlier.

We now consider the possibility that different rate estimates may be caused by incorrect assumptions used in the slip rate calculations (our third explanation). For example, offset reconstructions use landforms such as alluvial fans, but erosion may blur key features. In the case of the TR alluvial fan, the degree of incision by the ASCs into the TR alluvial fan can change the displacement and slip rate estimate by more than a factor of two. Since displacement is in the numerator for slip rate estimates, uncertainty in the displacement estimate has more of an effect on the rate estimate for younger alluvial fans. However, older alluvial fans may suffer more erosion, making it difficult to estimate accurate displacements for these features. Given the age ranges for the TR alluvial fan offset from OSL and TCN dating (5.0–14.0 ka), and a plausible maximum range of slip rates for the Calico Fault (1.4–12.0 mm/yr; Sauber *et al*. 1994; Oskin *et al*. 2007a; Selander 2015; McGill *et al*. 2015; this study), plausible displacements span a large range, from 7 to 168 m (Figure 14). If correct, this suggests that the ASC surface may not be incised exclusively into the TR alluvial fan.

Age determinations can also cause large uncertainties in slip rate estimates. TCN exposure dating techniques often result in large uncertainties due to a variety of geologic factors (Owen *et al*. 2011b), requiring data editing that could introduce systematic biases. While such editing is usually based on sound geological criteria, for example, relative ages derived from field observations, these assignments become more difficult for older alluvial fans. Wells *et al*. (1985) and Oskin *et al*. (2007a) note that criteria such as surface morphology and clast weathering tend to approach steady state with increasing age. Also, as alluvial fans get older, the possibility of surface disturbance increases (Owen *et al*. 2014). Northern hemisphere alluvial fans older than 300 ka have experienced three complete glacier-interglacial cycles, increasing the likelihood of surface disturbance by erosion and occasional minor deposition during wetter and cooler climate periods. This could result in ages that are too young.

While the ^{10}Be TCN technique used here has been widely employed for surface exposure dating, it does

rely on several assumptions for both pre- and post-formation history, including inheritance, erosion, and shielding. For the ALR alluvial fan, although most rock samples have age estimates of ~100 ka, we interpret these as underestimates of the true age of the landform because these ages are incompatible with soil, pavement, and carbonate rind development, and are well beyond the age estimate from the depth profile CalicoA. There are several explanations for ages that are too young, including shielding from cosmic rays due to sediment cover and later exhumation, toppling or rotation of the sampled clasts during erosional events, weathering (spallation), and bioturbation. The large range of age estimates (both rock samples and depth profiles) in both our study and other published studies reflects the multiple different surface processes operating on alluvial fan surfaces and clasts that can make ^{10}Be TCN data and other exposure age data challenging to interpret. We note, however, that our data exhibit no more scatter than other comparable studies (Figure 16).

Limited sampling can also lead to uncertainties and biases in geological slip rate estimates. Ideally, hundreds of samples would allow more rigorous assessment and statistical characterization of the various processes listed above that affect results. Unfortunately, this is well beyond current capabilities. For example, our preferred age estimate for the ALR alluvial fan is based on only the oldest rock sample; we interpret our other samples to be biased to younger ages. Similarly, in the study of Oskin et al. (2007a), the 'B' fan was assigned an age of 650 ± 100 ka based on a single sample, the one with the oldest cosmogenic ^{3}He exposure age (653.4 ± 19.8 ka; the second oldest age is 418.9 ± 12.6 ka), plus ^{40}Ar/^{39}Ar dating of two flows with ages of 770 ± 40 ka and 735 ± 9 ka, and all other ^{3}He dated samples yield much younger ages. The samples used for ^{40}Ar/^{39}Ar dating were also located several kilometres away from the source (Pipkin Basalt Flows, see Figure 2(a) in Oskin et al. (2007a). The ages of these samples may therefore represent upper bound for the formation age of the 'B' fan. In the same study, the 'K' fan was dated using both TCN ^{3}He and ^{10}Be. While ^{10}Be
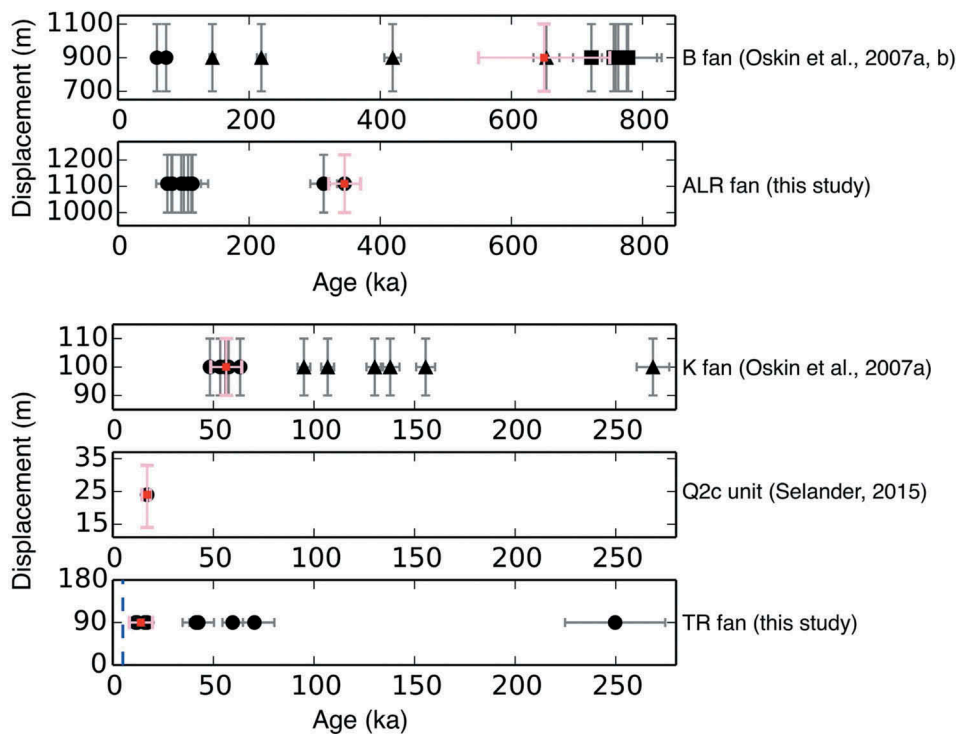

Figure 16. Ages of dated samples from Oskin et al. (2007a, 2007b), Selander (2015), and this study grouped in older (B and ALR) and younger (K, Q2c, TR) alluvial fans. Black dots with error bars show ^{10}Be dated ages, triangles with error bars show ^{3}He dated ages, squares with error bars show ^{40}Ar/^{39}Ar dated ages, note that some age error bars are smaller than the markers. Red squares with error bars show preferred estimates, note that Q2c unit age is from a depth profile. Note that 'B' fan studied by Oskin et al. (2007a, 2007b) uses data from three techniques: ^{40}Ar/^{39}Ar, ^{3}He and ^{10}Be. Outliers near the beginning and end of ^{40}Ar/^{39}Ar step-heating runs are omitted. Also note that the 90 m displacement for the TR alluvial fan is an estimate by aligning the northwestern edges of the TR alluvial fan surfaces (Figures 7(i–l) and 8(c,g)). Dashed blue line marks the TR alluvial fan age from OSL dating (5 ka). Locations of these fans are shown in Figure 15(b). Details of these ages are in Table 2.

dating gave consistent ages, [3]He dating results spanned a large range (more than a factor of 2) and hence were not used to define the exposure age of the 'K' fan. In both our study and the study of Oskin *et al.* (2007a) (and indeed most similar studies), the limited number of dated samples, the wide range of apparent ages, and the necessity of using selection criteria, increase the chances of biased results (Figure 16).

Young alluvial fans likely experienced less erosion but inheritance in TCN dating can be more significant due to their short exposure periods, as illustrated by the OSL results for the TR alluvial fan. Old alluvial fans likely experienced more erosion, but inheritance is dwarfed by the long post-formation exposure ages. Based on our data and several other studies (e.g. Oskin *et al.* 2007a; Frankel *et al.* 2011), the apparent ages of rock samples from an alluvial fan surface dated by TCN exposure age techniques tend to be distributed similarly to a chi-square distribution (Figure 17). For a young alluvial fan (a few tens of ka or younger; e.g. 'K' fan and the TR alluvial fan in Figure 16), apparent ages tend to skew towards older values because of inheritance (e.g. this study; Oskin *et al.* 2007a; Frankel *et al.* 2011). Hence the OSL results may be more reliable. In contrast, for older alluvial fans (hundreds ka or older; e.g., 'B' fan and the ALR alluvial fan in Figure 16), apparent ages tend to skew towards younger values because of disturbance and erosion (e.g. this study; Oskin *et al.* 2007a). While these considerations help in selecting reliable ages from an ensemble of apparent ages, it is clear that biases can occur.

These considerations suggest to us that the uncertainties of geologic slip rate estimate are often underestimated (see also Bird 2007; and Zechar and Frankel 2009). Even judicious selection criteria can lead to significant scatter in results (Figure 18). If Bird's (2007) criterion for the minimum number of independent estimates required for reliable rate determinations is

applied, even with our current study, we are far from having a robust picture for the slip rate history of individual faults in the Mojave section of the ECSZ, or the summed geologic rate across the shear zone.

Regarding on-fault slip rates (our fourth explanation), the slip rate of 3.2 ± 0.4 mm/yr from the ALR alluvial fan data is significantly faster than the estimate of 1.8 ± 0.3 by Oskin *et al.* (2007a) at a site that is only ~7 km away. However, these data could be reconciled if: (1) fault slip is almost completely localized onto the surface offset at ALR alluvial fan during its slip period; and (2) the offset studied by Oskin *et al.* (2007a) missed some off-fault deformation.

Dolan and Haravitch (2014) considered all faults in the Mojave section of the ECSZ as structurally immature, with strain not yet completely localized onto a narrow high strain fault core. Using their criteria, most ECSZ fault studies have underestimated slip rates. Dolan and Haravitch (2014) suggested that the slip rates of immature faults in the Mojave ECSZ have been underestimated by ~40%, even along straight, continuous, structurally simple sections of surface rupture. Using modified fault configurations, Herbert *et al.* (2014a) found that off-fault deformation accounts for 40 ± 23% of the total strain across the ECSZ, with higher percentages near places where faults terminate or bend. If the value of 40 ± 23% applies to most major faults in the Mojave region including the Calico Fault, then scaling Oskin *et al.*'s (2007a) result by this amount gives 3.0 ± 1.3 mm/yr, equivalent to our result within uncertainties. If this explanation is correct, it implies that surface geomorphic markers in this region record a variable portion of total displacement. In a similar environment, Fletcher *et al.* (2014) mapped surface ruptures caused by the M_w 7.2 El Mayor-Cucapah earthquake in 2010, finding that surface displacements varied along strike by orders of magnitude within a few kilometres along the trace of the fault.
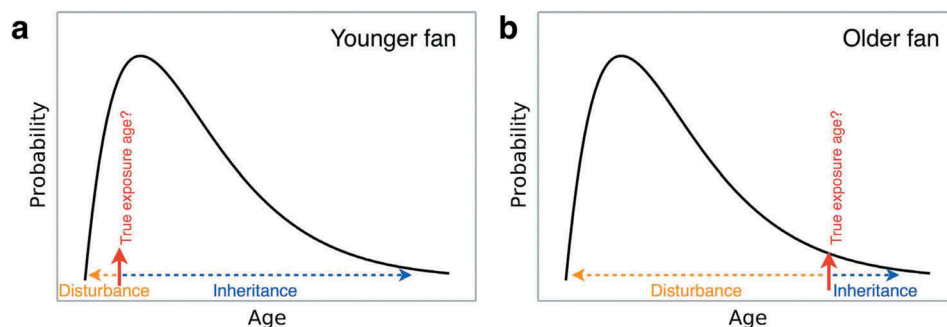

Figure 17. Hypothetical apparent age distribution for alluvial fans of different ages based on surface exposure dating using the TCN method. (a) Probability of sample ages from a relatively young fan, black curve shows a chi-square distribution reflecting increased likelihood of inheritance. (b) Probability of sample ages from a relatively old fan, black curve shows a chi-square distribution, reflecting increasing likelihood of surface disturbance. Note the scale of age in (b) is different from (a).
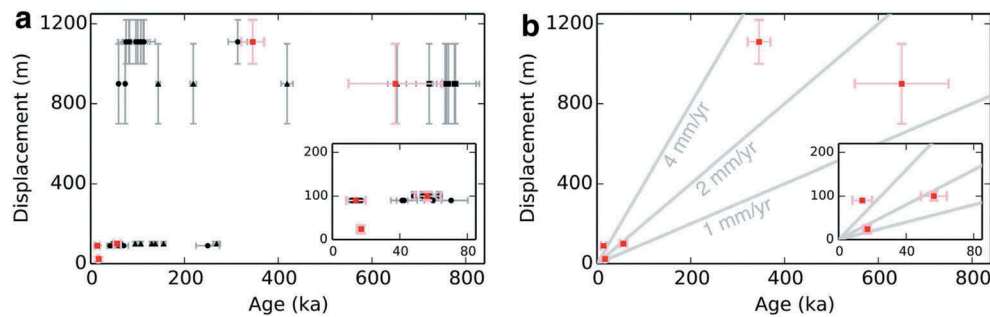
Figure 18. Age and displacement estimates for the Calico Fault from Oskin *et al.* (2007a, 2007b), Selander (2015) and this study. (a) Black dots with error bars show [10]Be dated ages, triangles with error bars show [3]He dated ages, squares with error bars show [40]Ar/[39]Ar dated ages. Red squares with error bars show preferred estimates. Note that some age error bars are smaller than the markers. Insert box expands data near origin. (b) Preferred estimates only, same as red square markers shown in (a). Grey lines show different mean slip rates for reference.

It should be noted that Oskin *et al.* (2007a) considered the possibility of off-fault deformation within a few hundred metres of the Calico fault. However, a related factor not considered by Oskin *et al.* (2007a) is the possibility of an unexposed and unmapped fault strand farther away that locally carries some of the slip at the more northern Calico site, but is not present at the location of the ALR and TR alluvial fans. Such unmapped strands may be especially problematic in the Mojave Desert, where widespread young alluvial deposits obscure the geomorphic effects of slow-moving strike slip faults and limit the number of clear offset markers. For example, Rockwell *et al.* (2000) noted that the southern part of the Landers earthquake rupture occurred on a previously unmapped fault.

The total displacement on a fault can help to constrain estimates of present day fault slip rate if the initiation age of the fault is known and if the slip rate history follows a simple evolutionary path, for example, a monotonic increase in rate through time until fault maturity is reached (Gourmelen *et al.* 2011). Total displacement may also help to address the issue of unaccounted off-fault deformation. Assuming it is estimated using an older, well-defined offset marker, total displacement should account for both on- and off-fault deformation. More generally, total displacement and slip rate history together help to define the evolutionary process of faulting and fault maturity.

Total displacement across the Calico Fault is estimated to be 9.8 km (Glazner *et al.* 2000; Oskin *et al.* 2007a). While we lack hard data on the age of slip initiation, some constraints are available. The most likely time for initiation of ECSZ faulting as a whole is sometime after the inland jump of the Pacific-North America plate boundary. Marine incursion into the northern Gulf of California is dated at 6.2 ± 0.2 Ma (Bennett *et al.* 2015). The ECSZ likely formed soon

after this time. Lee *et al.* (2009) suggested a 2.8 Ma initiation age for the Saline Valley–Hunter Mountain–Panamint Valley fault system north of the Garlock Fault, which may be kinematically related to the central faults of the Mojave ECSZ, including the Calico Fault. Dixon and Xie (2018) proposed a 4.1 Ma initiation age for the Calico Fault. Andrew and Walker (2017) proposed an initiation age for the Blackwater Fault, immediately northwest of the Calico Fault, at or after 3.8 Ma. In the analysis that follows, we investigate models with initiation ages between 2.8 and 6.2 Ma.

While firm conclusions cannot be drawn regarding slip rate and its relation to initiation age and total displacement, it is possible to rule out certain combinations of parameters. For example, both constant rate and constant acceleration models are inconsistent with initiation ages of 4.1 Ma or younger and present-day slip rate of 1.8 mm/yr (the total displacement would be smaller than observed; Figure 19(a)).

Gourmelen *et al.* (2011) proposed a damage growth model for young faults that results in an intermediate style of fault evolution, more rapidly than a constant acceleration model, but more slowly than a constant rate model (the latter implies essentially instantaneous acceleration at fault initiation). In the damage growth model, slip rate ramps up on time scales of several hundred thousand to several million years from zero at fault initiation to some steady state rate. The time from fault initiation to maximum acceleration is given by the Rayleigh scale parameter *S*, which occurs at roughly one half the final rate (Gourmelen *et al.* 2011). Figure 19(b) shows slip rate as a function of time for this model for a fault with 9.8 km displacement and an initiation age of 4.1 Ma, i.e., slightly older than the age proposed by Andrew and Walker (2017). Possible present-day rates range from 2.5 to 5.6 mm/yr. Figure 19(c) shows the range of permissible models for all initiation
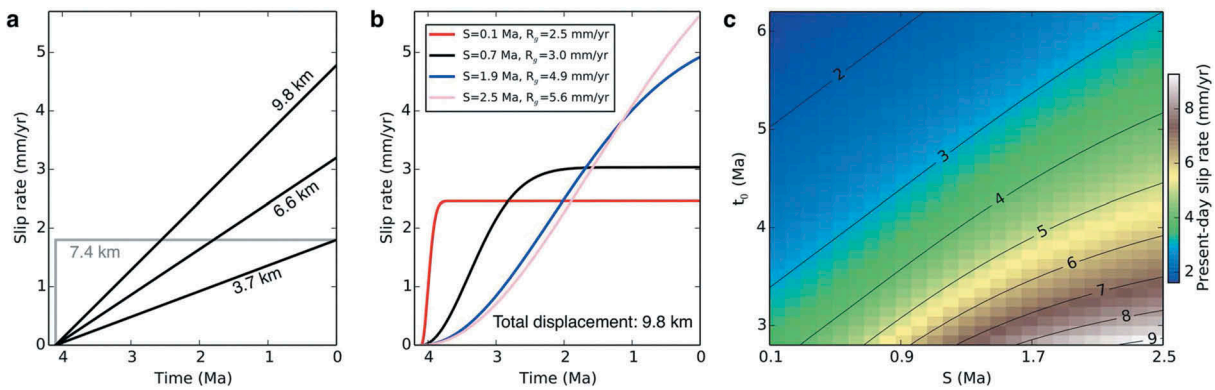
Figure 19. Slip rate models based on total displacement (9.8 km) and initiation age of the Calico Fault. (a) Slip rate estimates for a fault initiation age of 4.1 Ma. Grey line represents a constant slip rate of 1.8 mm/yr, the total displacement is 7.4 km. Each black line shows slip rate increasing with a constant acceleration: for present-day slip rates of 1.8 and 3.2 mm/yr, the total displacements are 3.7 and 6.6 km, respectively; to have a total displacement of 9.8 km, this model requires a present-day slip rate equal to 4.8 mm/yr. (b) Slip rate variation for an initiation age 4.1 Ma with different Rayleigh scale parameter S (time between fault initiation and maximum acceleration) based on a damage growth model (Gourmelen et al. 2011). Rg represents present-day slip rate. (c) Present-day slip rate based on plausible fault initiation age (t_0) and time between fault initiation and time of maximum acceleration (S). Numbers (in mm/yr) mark selected slip rate contour lines.

ages (t_0) between 2.8 and 6.2 Ma, using a range of values for S between 0.1 and 2.5 Ma. For a 2.8 Ma initiation age, possible values of present-day slip range from 3.5 to 9.3 mm/yr; For a 6.2 Ma initiation age, possible values of present-day slip rate range from 1.6 to 3.0 mm/yr.

If our new estimate of 3.2 ± 0.4 mm/yr is representative of the true slip rate of the Calico Fault (explanation number 4), it increases the cumulative geologic slip rate for the Mojave section of the ECSZ. If the 'slip deficit' noted in previous studies is largely due to fault immaturity, off-fault deformation, and underestimated slip, we can better approximate the overall geologic slip across the ECSZ by using our new result for the Calico Fault, and scaling on-fault geologic slip rates for remaining five major faults by some amount of off-fault deformation. There are various ways to do this. Using Herbert et al.'s (2014a) estimate of off-fault deformation (40 ± 23%) for the remaining five ECSZ faults, then the total geologic slip rate across the ECSZ becomes 10.5 ± 3.1 mm/yr (using the rates in Oskin et al. (2008) for the other five ECSZ faults; uncertainty in off-fault deformation of Herbert et al. (2014a) is considered), equivalent within uncertainties to the geodetically derived rate (Figure 20).

Given the importance of fault slip rate in seismic hazard estimates and fault evolution studies, the above discussion highlights the importance of continued research, and development of new approaches to fault slip rate determination over different time spans. For young alluvial fans such as the TR fan, perhaps the

use of landscape evolution models convolved with active faulting could better account for the effects of erosion and refine the displacement estimates, and hence the slip rate estimates (Figure 14).

We suggest that available data do not support a discrepancy between the summed geodetic rate across this section of the ECSZ and corresponding geologic rates averaged over the last few hundred thousand years, once the true uncertainty of these approaches has been considered. Since seismic hazard is closely related to fault slip rate, if discrepancies are observed, the faster rates (in this case based on the geodetic data) should be considered for seismic hazard estimates, until proven otherwise. This finding applies not only to the Mojave region, but also to other new or rapidly evolving plate boundary zones, where surface faults are immature, may be poorly exposed at the surface, and may have very low (or even zero) geologic slip rate estimates. The 2003 Bam earthquake in Iran, for example, was responsible for ~30,000 fatalities and occurred on a fault with limited surface exposure (Talebian et al. 2004; Fialko et al. 2005). Geologic studies on this fault, had they been done, would have indicated a slip rate of essentially zero. The tectonics of that region have clear similarities with the region studied here (Dixon and Xie 2018).

7. Conclusions

Our new slip rate estimate for the Calico Fault of 3.2 ± 0.4 mm/yr highlights the possibility that some fault slip rates in the Mojave Desert may have been
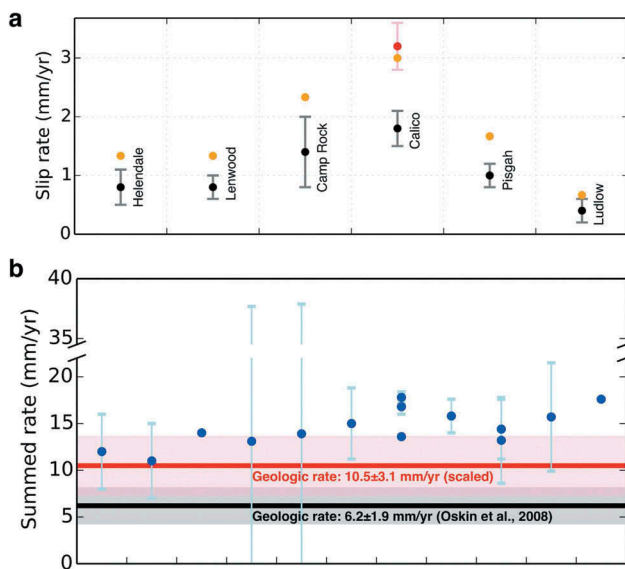
Figure 20. Comparison of geodetic slip rate and scaled geologic slip rate estimates. (a) Black dots with error bars (95% confidence) show on-fault geologic slip rate estimates of the six major active dextral faults (from west to east) from Oskin et al. (2007a), Oskin et al. (2008)). Red dot with error bar (also 95% confidence) shows our preferred slip rate estimate based on the ALR alluvial fan data. Yellow dots show scaled slip rates by assuming off-fault deformation accounts for 40±23% (Herbert et al. 2014a) of the total slip and have the same percentages for all individual faults, error bars omitted for clarity. (b) Blue dots with error bars show summed geodetic slip rate estimates, corresponding to references shown in Figure 2. Black line and grey area mark the summed geologic slip rate and uncertainty (95% confidence) from Oskin et al. (2008). Red line and pink area mark the updated summed geologic slip rate and uncertainty (95% confidence) based on our new slip rate estimated from the ALR alluvial fan, plus scaled slip rate estimates from Oskin et al. (2008), assuming off-fault deformation accounts for 40 ± 23% (Herbert et al. 2014a) of total slip. The new accumulative geologic rate across the ECSZ overlaps with most of the geodetic rate estimates within uncertainty.

under-estimated. This may be related to the limited number of studies in the region and the highly discontinuous and complex nature of the fault system. Among these immature young faults, where distributed deformation is common, total offset is not necessarily manifested as simple surface offset across a discrete fault plane; unmapped fault strands may be common. We also suggest that geologically determined slip rates have uncertainties that may be under-estimated. The overall ~10–12 mm/yr geodetic slip rate across the ECSZ is likely equivalent to the summed geologic rate across the region if our new estimate better represents the true slip rate along the Calico Fault system, if reasonable amounts of distributed deformation and unmapped faulting away from

the major faults are taken into account (Figure 20), and if realistic uncertainties are considered. Until the origins of the apparent rate discrepancy for the ECSZ are fully understood, the faster geodetic rate should be considered for seismic hazard estimates in the region.

Disclosure statement

No potential conflict of interest was reported by the authors.

ORCID

Surui Xie http://orcid.org/0000-0002-1484-0671
Elisabeth Gallant http://orcid.org/0000-0001-6841-3694
Paula M. Figueiredo http://orcid.org/0000-0002-5625-9295
Lewis A. Owen http://orcid.org/0000-0002-2525-5160
Craig Rasmussen http://orcid.org/0000-0003-4344-4800
Rocco Malservisi http://orcid.org/0000-0003-1767-8187
Timothy H. Dixon http://orcid.org/0000-0002-5127-0583

References

Adamiec, G., and Aitken, M.J., 1998, Dose-rate conversion factors: Update: Ancient tL, v. 16, no. 2, p. 37–50.

Aitken, M.J., 1998, An introduction to optical dating: The dating of quaternary sediments by the use of photon-stimulated luminescence: New York, Oxford University press, USA.

Amoroso, L., 2006, Age calibration of carbonate rind thickness in late Pleistocene soils for surficial deposit age estimation, Southwest USA: Quaternary Research, v. 65, no. 1, p. 172–178. doi:10.1016/j.yqres.2005.06.003

Andrew, J.E., and Walker, J.D., 2017, Path and amount of dextral fault slip in the Eastern California Shear Zone across the central Mojave Desert: Geological Society of America Bulletin, v. 129, no. 7–8, p. 855–868. doi:10.1130/B31527.1

Atwater, T., and Stock, J., 1998, Pacific-North America plate tectonics of the Neogene southwestern United States: An update: International Geology Review, v. 40, p. 375–402. doi:10.1080/00206819809465216

Becker, T.W., Hardebeck, J.L., and Anderson, G., 2005, Constraints on fault slip rates of the southern California plate boundary from GPS velocity and stress inversions: Geophysical Journal International, v. 160, p. 634–650. doi:10.1111/j.1365-246X.2004.02528.x

Bennett, R.A., Rodi, W., and Reilinger, R.E., 1996, Global positioning system constraints on fault slip rates in southern California and northern Baja, Mexico: Journal of Geophysical Research: Solid Earth, v. 101, no. B10, p. 21943–21960. doi:10.1029/96JB02488

Bennett, S.E.K., Oskin, M.E., Dorsey, R.J., Iriondo, A., and Kunk, M.J., 2015, Stratigraphy and structural development of the southwest Isla Tiburón marine basin: Implications for latest Miocene tectonic opening and flooding of the northern Gulf of California: Geosphere, v. 11, p. 977–1007. doi:10.1130/GES01153.1

Bird, P., 2007, Uncertainties in long-term geologic offset rates of faults: General principles illustrated with data from California and other western states: Geosphere, v. 3, no. 6, p. 577–595. doi:10.1130/GES00127.1

Chuang, R.Y., and Johnson, K.M., 2011, Reconciling geologic and geodetic model fault slip-rate discrepancies in Southern California: Consideration of nonsteady mantle flow and lower crustal fault creep: Geology, v. 39, no. 7, p. 627–630. doi:10.1130/G32120.1

Cooke, M.L., and Dair, L.C., 2011, Simulating the recent evolution of the southern big bend of the San Andreas fault, southern California: Journal of Geophysical Research: Solid Earth, v. 116, no. B4. doi:10.1029/2010JB007835

DeMets, C., and Dixon, T.H., 1999, New kinematic models for Pacific-North America motion from 3 Ma to present, I: Evidence for steady motion and biases in the NUVEL-1A model: Geophysical Research Letters, v. 26, no. 13, p. 1921–1924. doi:10.1029/1999GL900405

DeMets, C., and Merkouriev, S., 2016, High-resolution reconstructions of Pacific–North America plate motion: 20 Ma to present: Geophysical Journal International, v. 207, no. 2, p. 741–773. doi:10.1093/gji/ggw305

Dixon, T.H., Miller, M., Farina, F., Wang, H., and Johnson, D., 2000, Present-day motion of the Sierra Nevada block and some tectonic implications for the Basin and Range province, North American Cordillera: Tectonics, v. 19, no. 1, p. 1–24. doi:10.1029/1998TC001088

Dixon, T.H., Norabuena, E., and Hotaling, L., 2003, Paleoseismology and Global Positioning System: Earthquake-cycle effects and geodetic versus geologic fault slip rates in the Eastern California shear zone: Geology, v. 31, no. 1, p. 55–58. doi:10.1130/0091-7613(2003)031<0055:PAGPSE>2.0.CO;2

Dixon, T.H., Robaudo, S., Lee, J., and Reheis, M.C., 1995, Constraints on present-day basin and range deformation from space geodesy: Tectonics, v. 14, no. 4, p. 755–772. doi:10.1029/95TC00931

Dixon, T.H., and Xie, S., 2018, A kinematic model for the evolution of the Eastern California Shear Zone and Garlock Fault, Mojave Desert, California: Earth and Planetary Science Letters, v. 494, p. 60–68. doi:10.1016/j.epsl.2018.04.050

Dokka, R.K., 1983, Displacements on late Cenozoic strike-slip faults of the central Mojave Desert, California: Geology, v. 11, no. 5, p. 305–308. doi:10.1130/0091-7613(1983)11<305:DOLCSF>2.0.CO;2

Dokka, R.K., and Travis, C.J., 1990a, Late Cenozoic strike-slip faulting in the Mojave Desert, California: Tectonics, v. 9, no. 2, p. 311–340. doi:10.1029/TC009i002p00311

Dokka, R.K., and Travis, C.J., 1990b, Role of the eastern California shear zone in accommodating Pacific-North American plate motion: Geophysical Research Letters, v. 17, no. 9, p. 1323–1326. doi:10.1029/GL017i009p01323

Dolan, J.F., Bowman, D.D., and Sammis, C.G., 2007, Long-range and long-term fault interactions in Southern California: Geology, v. 35, no. 9, p. 855–858. doi:10.1130/G23789A.1

Dolan, J.F., and Haravitch, B.D., 2014, How well do surface slip measurements track slip at depth in large strike-slip earthquakes? The importance of fault structural maturity in controlling on-fault slip versus off-fault surface deformation: Earth and Planetary Science Letters, v. 388, p. 38–47. doi:10.1016/j.epsl.2013.11.043

Dorn, R.I., 2009, The role of climatic change in alluvial fan development, in Geomorphology of desert environments, 2nd ed: Dordrecht, Springer, p. 723–742.

Duncan, J.A., King, G.E., and Duller, G.A.T., 2015, DTAC: Dose rate and age calculator for trapped charge dating: Quaternary Geochronology, v. 28, p. 54–61. doi:10.1016/j.quageo.2015.03.012

Evans, E.L., Thatcher, W.R., Pollitz, F.F., and Murray, J.R., 2016, Persistent slip rate discrepancies in the eastern California (USA) shear zone: Geology, v. 44, no. 9, p. 691–694. doi:10.1130/G37967.1

Fialko, Y., Sandwell, D., Simon, M., and Rosen, P., 2005, Three-dimensional deformation caused by the Bam, Iran, earthquake and the origin of shallow slip deficit: Nature, v. 435, p. 295–299. doi:10.1038/nature03425

Fletcher, J.M., Teran, O.J., Rockwell, T.K., Oskin, M.E., Hudnut, K.W., Mueller, K.J., Spelz, R.M., Akciz, S.O., Masana, E., Faneros, G., and Fielding, E.J., 2014, Assembly of a large earthquake from a complex fault system: Surface rupture kinematics of the 4 April 2010 El Mayor–Cucapah (Mexico) Mw 7.2 earthquake: Geosphere, v. 10, no. 4, p. 797–827. doi:10.1130/GES00933.1

Frankel, K.L., Glazner, A.F., Kirby, E., Monastero, F.C., Strane, M.D., Oskin, M.E., Unruh, J.R., Walker, J.D., Anandakrishnan, S., Bartley, J.M., Coleman, D.S., Dolan, J.F., Finkel, R.C., Greene, D., Kylander-Clark, A., Marrero, S., Owen, L.A., and Phillips, F., 2008, Active tectonics of the eastern California shear zone, in Duebendorfer, E.M., and Smith, E.I., eds., Field guide to plutons, volcanoes, faults, reefs, dinosaurs, and possible glaciation in selected areas of Arizona, California, and Nevada: Geological Society of America Field Guides, Vol. 11 p. 43–81. doi:10.1130/2008.fld011(03)

Frankel, K.L., Dolan, J.F., Owen, L.A., Ganev, P., and Finkel, R.C., 2011, Spatial and temporal constancy of seismic strain release along an evolving segment of the Pacific–North America plate boundary: Earth and Planetary Science Letters, v. 304, no. 3–4, p. 565–576. doi:10.1016/j.epsl.2011.02.034

Frankel, K.L., Owen, L.A., Dolan, J.F., Knott, J.R., Lifton, Z.M., Finkel, R.C., and Wasklewicz, T., 2015, Timing and rates of Holocene normal faulting along the Black Mountains fault zone, Death Valley, USA: Lithosphere, v. 8, no. 1, p. 3–22. doi:10.1130/L464.1

Fulton, P.M., Schmalzle, G., Harris, R., and Dixon, T.H., 2010, Reconciling patterns of interseismic strain accumulation with thermal observations across the Carrizo section of

the San Andreas Fault: Earth and Planetary Science Letters, v. 300, p. 402–406. doi:10.1016/j.epsl.2010.10.024

Gan, W., Svarc, J.L., Savage, J.C., and Prescott, W.H., 2000, Strain accumulation across the Eastern California Shear Zone at latitude 36 30′ N: Journal of Geophysical Research: Solid Earth, v. 105, no. B7, p. 16229–16236. doi:10.1029/2000JB900105

Ganev, P.N., Dolan, J.F., Blisniuk, K., Oskin, M., and Owen, L.A., 2010, Paleoseismologic evidence for multiple Holocene earthquakes on the Calico Fault: Implications for earthquake clustering in the Eastern California shear zone: Lithosphere, v. 2, no. 4, p. 287–298. doi:10.1130/L82.1

Glazner, A.F., Bartley, J.M., and Sanner, W.K., 2000, Nature of the southwestern boundary of the central Mojave Tertiary province, Rodman Mountains, California: Geological Society of America Bulletin, v. 112, p. 34–44. doi:10.1130/0016-7606 (2000)112<34:NOTSBO>2.0.CO;2

Gosse, J.C., and Phillips, F.M., 2001, Terrestrial in situ cosmogenic nuclides: Theory and application: Quaternary Science Reviews, v. 20, no. 14, p. 1475–1560. doi:10.1016/S0277-3791(00)00171-2

Gourmelen, N., Dixon, T.H., Amelung, F., and Schmalzle, G., 2011, Acceleration and evolution of faults: An example from the Hunter Mountain–Panamint Valley fault zone, Eastern California: Earth and Planetary Science Letters, v. 301, no. 1, p. 337–344. doi:10.1016/j.epsl.2010.11.016

Gray, H.J., Owen, L.A., Dietsch, C., Beck, R.A., Caffee, M.A., Finkel, R.C., and Mahan, S.A., 2014, Quaternary landscape development, alluvial fan chronology and erosion of the Mecca Hills at the southern end of the San Andreas fault zone: Quaternary Science Reviews, v. 105, p. 66–85. doi:10.1016/j.quascirev.2014.09.009

Haddon, E.K., Amos, C.B., Zielke, O., Jayko, A.S., and Bürgmann, R., 2016, Surface slip during large Owens Valley earthquakes: Geochemistry, Geophysics, Geosystems, v. 17, no. 6, p. 2239–2269. doi:10.1002/2015GC006033

Harden, J.W., 1982, A quantitative index of soil development from field descriptions: Examples from a chronosequence in central California: Geoderma, v. 28, no. 1, p. 1–28. doi:10.1016/0016-7061(82)90037-4

Harden, J.W., Taylor, E.M., Hill, C., Mark, R.K., McFadden, L.D., Reheis, M.C., Sowers, J.M., and Wells, S.G., 1991, Rates of soil development from four soil chronosequences in the southern Great Basin: Quaternary Research, v. 35, no. 3–Part1, p. 383–399. doi:10.1016/0033-5894(91)90052-7

Hedrick, K.A., Owen, L.A., Chen, J., Robinson, A., Yuan, Z., Yang, X., Imrecke, D.B., Li, W., Caffee, M.W., Schoenbohm, L.M., and Zhang, B., 2017, Quaternary history and landscape evolution of a high-altitude intermountain basin at the western end of the Himalayan-Tibetan orogen, Waqia Valley, Chinese Pamir: Geomorphology, v. 284, p. 156–174. doi:10.1016/j.geomorph.2016.09.002

Herbert, J.W., Cooke, M.L., and Marshall, S.T., 2014b, Influence of fault connectivity on slip rates in southern California: Potential impact on discrepancies between geodetic derived and geologic slip rates: Journal of Geophysical Research: Solid Earth, v. 119, no. 3, p. 2342–2361. doi:10.1002/2013JB010472

Herbert, J.W., Cooke, M.L., Oskin, M., and Difo, O., 2014a, How much can off-fault deformation contribute to the slip rate discrepancy within the eastern California shear zone?: Geology, v. 42, no. 1, p. 71–75. doi:10.1130/G34738.1

Hidy, A., 2013, Cosmogenic nuclide quantification of paleo-fluvial sedimentation rates in response to climate change Ph.D Thesis: Halifax, Dalhousie University.

Hidy, A.J., Gosse, J.C., Pederson, J.L., Mattern, J.P., and Finkel, R.C., 2010, A geologically constrained Monte Carlo approach to modeling exposure ages from profiles of cosmogenic nuclides: An example from Lees Ferry, Arizona: Geochemistry, Geophysics, Geosystems, v. 11, no. 9. doi:10.1029/2010GC003084

Kreemer, C., Holt, W.E., and Haines, A.J., 2003, An integrated global model of present-day plate motions and plate boundary deformation: Geophysical Journal International, v. 154, no. 1, p. 8–34. doi:10.1046/j.1365-246X.2003.01917.x

Lawson, M.J., Roder, B.J., Stang, D.M., and Rhodes, E.J., 2012, Characteristics of quartz and feldspar from southern California, USA: Radiation Measurements, v. 47, p. 830–836. doi:10.1016/j.radmeas.2012.03.025

Lease, R.O., McQuarrie, N., Oskin, M., and Leier, A., 2009, Quantifying dextral shear on the Bristol-Granite Mountains fault zone: Successful geologic prediction from kinematic compatibility of the Eastern California Shear Zone: Journal of Geology, v. 117, no. 1, p. 37–53. doi:10.1086/593320

Lee, J., Stockli, D.F., Owen, L.A., Finkel, R.C., and Kislitsyn, R., 2009, Exhumation of the inyo mountains, california: implications for the timing of extension along the western boundary of the basin and range province and distribution of dextral fault slip rates across the eastern california shear zone: tectonics, v. 28, no. 1. doi: 10.1029/2008TC002295

Lifton, Z.M., Newman, A.V., Frankel, K.L., Johnson, C.W., and Dixon, T.H., 2013, Insights into distributed plate rates across the Walker Lane from GPS geodesy: Geophysical Research Letters, v. 40, no. 17, p. 4620–4624. doi:10.1002/grl.50804

Liu, S., Shen, Z.K., and Bürgmann, R., 2015, Recovery of secular deformation field of Mojave shear zone in southern California from historical terrestrial and GPS measurements: Journal of Geophysical Research: Solid Earth, v. 120, no. 5, p. 3965–3990. doi:10.1002/2015JB011941

Loveless, J.P., and Meade, B.J., 2011, Stress modulation on the San Andreas fault by interseismic fault system interactions: Geology, v. 39, no. 11, p. 1035–1038. doi:10.1130/G32215.1

Malservisi, R., Dixon, T.H., and LaFemina, P., 2003, Holocene slip rate of the Wasatch fault zone, Utah, from geodetic data: Geophysical Research Letters, v. 30. doi:10.1029/2003GL017408

Malservisi, R., Furlong, K.P., and Dixon, T.H., 2001, Influence of the earthquake cycle and lithospheric rheology on the dynamics of the eastern California shear zone: Geophysical Research Letters, v. 28, no. 14, p. 2731–2734. doi:10.1029/2001GL013311

McCaffrey, R., 2005, Block kinematics of the Pacific–North America plate boundary in the southwestern United States from inversion of GPS, seismological, and geologic data: Journal of Geophysical Research: Solid Earth, v. 110, no. B7. doi:10.1029/2004JB003307

McClusky, S.C., Bjornstad, S.C., Hager, B.H., King, R.W., Meade, B.J., Miller, M.M., and Souter, B.J., 2001, Present day kinematics of the eastern California shear zone from a geodetically constrained block model: Geophysical Research Letters, v. 28, no. 17, p. 3369–3372. doi:10.1029/2001GL013091

McDonald, E.V., McFadden, L.D., and Wells, S.G., 2003, Regional response of alluvial fans to the Pleistocene-Holocene climatic transition, Mojave Desert, California, in Enzel, Y., Wells, S.G.,

and Lancaster, N., eds., Paleoenvironments and paleohydrology of the Mojave and southern Great Basin Deserts: Boulder, Colorado, Geological Society of America Special Paper 368, p. 189–205.

McGill, S.F., Spinler, J.C., McGill, J.D., Bennett, R.A., Floyd, M.A., Fryxell, J.E., and Funning, G.J., 2015, Kinematic modeling of fault slip rates using new geodetic velocities from a transect across the Pacific-North America plate boundary through the San Bernardino Mountains, California: Journal of Geophysical Research: Solid Earth, v. 120, no. 4, p. 2772–2793. doi:10.1002/2014JB011459

McQuarrie, N., and Wernicke, B.P., 2005, An animated tectonic reconstruction of southwestern North America since 36 Ma: Geosphere, v. 1, no. 3, p. 147–172. doi:10.1130/GES00016.1

Meade, B.J., and Hager, B.H., 2005, Block models of crustal motion in southern California constrained by GPS measurements: Journal of Geophysical Research: Solid Earth, v. 110, no. B3. doi:10.1029/2004JB003209

Mejdahl, V., 1979, Thermoluminescence dating: Beta-dose attenuation in quartz grains: Archaeometry, v. 21, no. 1, p. 61–72. doi:10.1111/j.1475-4754.1979.tb00241.x

Miller, D.M., Schmidt, K.M., Mahan, S.A., McGeehin, J.P., Owen, L.A., Barron, J.A., Lehmkuhl, F., and Löhrer, R., 2010, Holocene landscape response to seasonality of storms in the Mojave Desert: Quaternary International, v. 215, no. 1–2, p. 45–61. doi:10.1016/j.quaint.2009.10.001

Miller, M.M., Johnson, D.J., Dixon, T.H., and Dokka, R.K., 2001, Refined kinematics of the Eastern California shear zone from GPS observations, 1993–1998: Journal of Geophysical Research: Solid Earth, v. 106, no. B2, p. 2245–2263. doi:10.1029/2000JB900328

Minster, J.B., and Jordan, T.H., 1987, Vector constraints on western U.S. deformation from space geodesy, neotectonics, and plate motions: Journal of Geophysical Research, v. 92, no. B6, p. 4798–4804. doi:10.1029/JB092iB06p04798

Murray, A.S., and Olley, J.M., 2002, Precision and accuracy in the optically stimulated luminescence dating of sedimentary quartz: A status review: Geochronometria, v. 21, no. 1, p. 1–16.

Murray, A.S., and Wintle, A.G., 2000, Luminescence dating of quartz using an improved single-aliquot regenerative-dose protocol: Radiation Measurements, v. 32, no. 1, p. 57–73. doi:10.1016/S1350-4487(99)00253-X

Oldow, J.S., Geissman, J.W., and Stockli, D.F., 2008, Evolution and strain reorganization within late Neogene structural stepovers linking the central Walker Lane and northern Eastern California shear zone, western Great Basin: International Geology Review, v. 50, no. 3, p. 270–290. doi:10.2747/0020-6814.50.3.270

Oskin, M., and Iriondo, A., 2004, Large-magnitude transient strain accumulation on the Blackwater fault, Eastern California shear zone: Geology, v. 32, no. 4, p. 313–316. doi:10.1130/G20223.1

Oskin, M., Perg, L., Blumentritt, D., Mukhopadhyay, S., and Iriondo, A., 2007a, Slip rate of the Calico Fault: Implications for geologic versus geodetic rate discrepancy in the eastern California shear zone: Journal of Geophysical Research: Solid Earth, v. 112, no. B3. doi:10.1029/2006JB004451

Oskin, M., Perg, L., Blumentritt, D., Mukhopadhyay, S., and Iriondo, A., 2007b, Correction to "Slip rate of the Calico Fault: Implications for geologic versus geodetic rate discrepancy in the Eastern California Shear Zone": Journal of Geophysical Research, v. 112, p. B07406. doi:10.1029/2007JB005222

Oskin, M., Perg, L., Shelef, E., Strane, M., Gurney, E., Singer, B., and Zhang, X., 2008, Elevated shear zone loading rate during an earthquake cluster in eastern California: Geology, v. 36, no. 6, p. 507–510. doi:10.1130/G24814A.1

Oskin, M., and Stock, J., 2003, Pacific–North America plate motion and opening of the Upper Delfín basin, northern Gulf of California, Mexico: Geological Society of America Bulletin, v. 115, no. 10, p. 1173–1190. doi:10.1130/B25154.1

Owen, L.A., Bright, J., Finkel, R.C., Jaiswal, M.K., Kaufman, D., Mahan, S., Schneider, J.S., Sharp, W., Singhvi, A.K., and Warren, C.N., 2007, Numerical dating of a Late Quaternary spit-shoreline complex at the northern end of Silver Lake, Mojave Desert, California: Quaternary International, v. 166, p. 87–100. doi:10.1016/j.quaint.2007.01.001

Owen, L.A., Clemmens, S.J., Finkel, R.C., and Gray, H., 2014, Late Quaternary alluvial fans at the eastern end of the San Bernardino Mountains, Southern California: Quaternary Science Reviews, v. 87, p. 114–134. doi:10.1016/j.quascire2014.01.003

Owen, L.A., Davis, T., Caffee, M.W., Budinger, F., and Nash, D., 2011a, Surface ages and rates of erosion at the Calico Archaeological Site in the Mojave Desert, Southern California: Geomorphology, v. 125, no. 1, p. 40–50. doi:10.1016/j.geomorph.2010.08.013

Owen, L.A., Frankel, K.L., Knott, J.R., Reynhout, S., Finkel, R.C., Dolan, J.F., and Lee, J., 2011b, Beryllium-10 terrestrial cosmogenic nuclide surface exposure dating of Quaternary landforms in Death Valley: Geomorphology, v. 125, p. 541–557. doi:10.1016/j.geomorph.2010.10.024

Peltzer, G., Crampé, F., Hensley, S., and Rosen, P., 2001, Transient strain accumulation and fault interaction in the Eastern California shear zone: Geology, v. 29, no. 11, p. 975–978. doi:10.1130/0091-7613(2001)029<0975:TSAAFI>2.0.CO;2

Petersen, M.D., Moschetti, M.P., Powers, P.M., Mueller, C.S., Haller, K.M., Frankel, A.D., Zeng, Y., Rezaeian, S., Harmsen, S.C., Boyd, O.S., and Field, N., 2015, The 2014 United States national seismic hazard model: Earthquake Spectra, v. 31, no. S1, p. S1–S30. doi:10.1193/120814EQS210M

Prescott, J.R., and Hutton, J.T., 1994, Cosmic ray contributions to dose rates for luminescence and ESR dating: Large depths and long-term time variations: Radiation Measurements, v. 23, no. 2–3, p. 497–500. doi:10.1016/1350-4487(94)90086-8

Rockwell, T.K., Lindvall, S., Herzberg, M., Murbach, D., Dawson, T., and Berger, G., 2000, Paleoseismology of the Johnson Valley, Kickapoo, and Homestead Valley faults: Clustering of earthquakes in the eastern California shear zone: Bulletin of the Seismological Society of America, v. 90, no. 5, p. 1200–1236. doi:10.1785/0119990023

Sauber, J., Thatcher, W., Solomon, S.C., and Lisowski, M., 1994, Geodetic slip rate for the eastern California shear zone and the recurrence time of Mojave Desert earthquakes: Nature, v. 367, no. 6460, p. 264–266. doi:10.1038/367264a0

Savage, J.C., Lisowski, M., and Prescott, W.H., 1990, An apparent shear zone trending north-northwest across the Mojave Desert into Owens Valley, eastern California: Geophysical Research Letters, v. 17, p. 2113–2116. doi:10.1029/GL017i012p02113

Schmalzle, G., Dixon, T.H., Malservisi, R., and Govers, R., 2005, Strain accumulation across the Carrizo Segment of the San Andreas Fault, California: Impact of laterally varying crustal properties: Journal of Geophysical Research, v. 111, p. B05403. doi:10.1029/2005JB003843

Schoenegerger, P.J., Wysock, D.A., Benham, E.C., and Soil Survey Staff, 2012, Field book for describing and sampling soils, Version 3.0. Natural Resources Conservation Service: Lincoln, NE, National Soil Survey Center.

Selander, J.A., 2015, Mechanisms of strain transfer along strike-slip faults: Examples from the Mojave Desert, California [Ph.D Thesis]: Davis, University of California.

Sella, G.F., Dixon, T.H., and Mao, A., 2002, REVEL: A model for recent plate velocities from space geodesy: Journal of Geophysical Research: Solid Earth, v. 107, no. B4. doi:10.1029/2000JB000033

Shelef, E., and Oskin, M., 2010, Deformation processes adjacent to active faults: Examples from eastern California: Journal of Geophysical Research: Solid Earth, v. 115, no. B5. doi:10.1029/2009JB006289

Shen, Z.K., King, R.W., Agnew, D.C., Wang, M., Herring, T.A., Dong, D., and Fang, P., 2011, A unified analysis of crustal motion in Southern California, 1970–2004: The SCEC crustal motion map: Journal of Geophysical Research: Solid Earth, v. 116, no. B11. doi:10.1029/2011jb008549

Shepard, C., Pelletier, J.D., Schaap, M.G., and Rasmussen, C., 2018, Signatures of obliquity and eccentricity in soil chronosequences: Geophysical Research Letters, v. 45. doi:10.1029/2018GL078583

Singhvi, A.K., and Porat, N., 2008, Impact of luminescence dating on geomorphological and palaeoclimate research in drylands: Boreas, v. 37, no. 4, p. 536–558. doi:10.1111/j.1502-3885.2008.00058.x

Soil Survey Staff, 2014, Keys to soil taxonomy, 12th ed: United States Department of Agriculture, Natural Resources Conservation Service.

Spinler, J.C., Bennett, R.A., Anderson, M.L., McGill, S.F., Hreinsdóttir, S., and McCallister, A., 2010, Present-day strain accumulation and slip rates associated with southern San Andreas and eastern California shear zone faults: Journal of Geophysical Research: Solid Earth, v. 115, no. B11. doi:10.1029/2010JB007424

Stirling, M.W., Wesnousky, S.G., and Shimazaki, K., 1996, Fault trace complexity, cumulative slip, and the shape of the magnitude-frequency distribution for strike-slip faults: A global survey: Geophysical Journal International, v. 124, no. 3, p. 833–868. doi:10.1111/j.1365-246X.1996.tb05641.x

Talebian, M., Fielding, E.J., Funning, G.J., Ghorashi, M., Jackson, J., Nazari, H., Parsons, B., Priestley, K., Rosen, P.A., Walker, R., and Wright, T.J., 2004, The 2003 Bam (Iran) earthquake: Rupture of a blind strike-slip fault: Geophysical Research Letters, v. 31, no. 11. doi:10.1029/2004GL020058

U.S. Geological Survey and California Geological Survey, 2006, Quaternary fault and fold database for the United States: http://earthquakes.usgs.gov/hazards/qfaults/ (accessed 16 June 2016).

Ward, S.N., 1990, Pacific-North America Plate motions: New results from very long baseline interferometry: Journal of Geophysical Research: Solid Earth, v. 95, no. B13, p. 21965–21981. doi:10.1029/JB095iB13p21965

Wells, S.G., Dohrenwend, J.C., McFadden, L.D., Turrin, B.D., and Mahrer, K.D., 1985, Late Cenozoic landscape evolution on lava flow surfaces of the Cima volcanic field, Mojave Desert, California: Geological Society of America Bulletin, v. 96, no. 12, p. 1518–1529. doi:10.1130/0016-7606(1985)96<1518:LCLEOL>2.0.CO;2

Wesnousky, S.G., 1988, Seismological and structural evolution of strike-slip faults: Nature, v. 335, no. 6188, p. 340–343. doi:10.1038/335340a0

Wesnousky, S.G., 2005, Active faulting in the Walker Lane: Tectonics, v. 24, no. 3. doi:10.1029/2004TC001645

Ye, J., and Liu, M., 2017, How fault evolution changes strain partitioning and fault slip rates in southern California: Results from geodynamic modeling: Journal of Geophysical Research: Solid Earth. doi:10.1002/2017JB014325

Zechar, J.D., and Frankel, K.L., 2009, Incorporating and reporting uncertainties in fault slip rates: Journal of Geophysical Research: Solid Earth, v. 114, p. B12. doi:10.1029/2009JB006325

Zielke, O., Klinger, Y., and Arrowsmith, J.R., 2015, Fault slip and earthquake recurrence along strike-slip faults—Contributions of high-resolution geomorphic data: Tectonophysics, v. 638, p. 43–62. doi:10.1016/j.tecto.2014.11.004